Modelling the effects of slip on dipole-wall collision problems using a lattice Boltzmann equation method

S. Mohammed,[1, a)] D. I. Graham,[2, b)] and T. Reis[3, c)]

[1)]*College of Science, Department of Mathematics, University of Baghdad, Al-Jadiria, Baghdad, 10001, Iraq*

[2)]*School of Engineering, Computing and Mathematics, Plymouth University, Plymouth, PL4 8AA, UK*

[3)]*School of Computing and Mathematical Sciences, University of Greenwich, London, SE10 9LS, UK*

(Dated: 24 January 2020)

We study the physics of flow due to the interaction between a viscous dipole and boundaries that permit slip. This includes partial and free slip, and interactions near corners. The problem is investigated by using a two relaxation time lattice Boltzmann equation (TRT-LBE) with moment-based boundary conditions. Navier-slip conditions, which involve gradients of the velocity, are formulated and applied locally. The implementation of free-slip conditions with the moment-based approach is discussed. Collision angles of $0°$, $30°$ and $45°$ are investigated. Stable simulations are shown for Reynolds numbers between 625 and 10000 and various slip lengths. Vorticity generation on the wall is shown to be affected by slip length, angle of incidence, and Reynolds number. An increase in wall slippage causes a reduction in the number of higher-order dipoles created. This leads to a decrease in the magnitude of the entropy peaks and reduces the dissipation of energy. The dissipation of the energy and its relation to the enstrophy are also investigated theoretically, confirming quantitatively how the presence of slip modifies this relation.

I. INTRODUCTION

The interactions between dipoles and no-slip boundaries have been investigated in numerous studies to aid our understanding of vortex dynamics in bounded domains, with important applications such as trailing vorticies from aircrafts interacting with the ground and geophysical vorticies interacting with coasts and landscapes[1–6]. The problem of high Reynolds number (Re) voticies rebounding from surfaces that permit slip is less well studied and understood but has received some attention, particularly in recent years, mainly because of the potential for slip surfaces to reduce drag and voricity generation. Early research on vortex dynamics in bounded domains using free-slip conditions was conducted by Barker *et al.*[7] and Saffman[8] in the context of aircraft trailing vorticies. The Navier-slip boundary condition[9] for partial slip with slip lengths that are independent of Reynolds number have been used to model and simulate incompressible flow over textured superhydrophobic surfaces. The application here is skin friction drag reduction and the slip length depends on the geometry and the surface texture of the boundary[10]. Jäger and Mikelić[11] studied Couette flow with rough boundaries and entered the surface roughness via the slip length. They showed that the effective slip reduced the tangential drag. Rastan *et al*[12] investigated the effect of slip lengths for turbulent flow over coated hydrofoils with slip boundary conditions at high Reynolds numbers. They found a very large reduction in frictional and pressure drag when they increased the slip length. As discussed by Fairhall *et. al*[13], surface roughness on hydrophobic surfaces can entrap gas pockets which a flowing

fluid can slip over. They used the Navier-slip condition to model this phenomena and analysed its effect on turbulent flows over hydrophobic surfaces. Ibrahim *et al*[14] numerically investigated flow over smooth and drag-reducing surfaces using slip boundary conditions and concluded that the streamwise slip length sets the virtual origin of the mean flow while the wall normal and spanwise slip lengths set the virtual origin of the turbulence. Farge *et al.*[15] numerically investigated turbulent structures in incompressible flow by simulating a dipole colliding with a wall which has slip boundary conditions with slip lengths proportional to Re^{-1}. Their results suggest the existence of energy dissipating structures that persist in the inviscid limit (corresponding to free slip). Sutherland[16,17] used a volume penalisation method to perform a detailed numerical study of the rate of energy dissipation when a dipole collides with a wall in a bounded domain up to a Reynolds number of 1252. It was shown that when the dipole hits a slip wall, the distance between the two monopoles that are formed after the collision is wider compared with the no-slip case and the number of rebounds and subsequent collisions with the wall is reduced. Thus it seems that the induction of additional dipoles is more energetic when the dipole hits a no-slip wall than when it hits a wall that allows slip. That is, the slip length controls the number of vortices that are produced in the boundary layer for a given Re.

Slip and stress-free conditions have been utilised to study geophysical flows[18,19]. During a hurricane or tornado, vortices may be modelled as sliding along the ground with free-slip condition[20] although Fiedler[21] argues that a partial slip condition can better account for surface roughness effects. Carnevale *et al.*[22] carried out numerical and laboratory experiments on dipole collision with no-slip and free-slip walls. They found a purely inviscid mechanism for vortex generation in coastal dynamics. In aeroacoustics velocity boundary conditions and the angle of collision between voticies

---

[a)]Electronic mail: seemaa.mohammed84@gmail.com

[b)]Electronic mail: D.Graham@plymouth.ac.uk

[c)]Electronic mail: T.Reis@Greenwich.ac.uk

and boundaries influences the sound pressure radiated by the collision[23–26].

Previous numerical investigations into dipole-wall collision problems were performed using traditional methods of computational fluid dynamics (CFD) that discretise the macroscopic equations of motion, namely the Navier-Stokes equations using, for example, finite difference, finite volume, finite element, or spectral methods. Numerical difficulties or computational expense is common at high Reynolds numbers and complicated boundary conditions such as the Navier-slip condition that are expressed as gradients. The lattice Boltzmann Method (LBM), on the other hand, is based on a velocity space truncation of Boltzmann's equation from kinetic theory and is now considered a viable alternative CFD method[27,28]. Unlike the more traditional CFD approaches, which have nonlinear convective terms, the LBM has a simpler linear advection term. All of the nonlinearities of the LBM are reserved for a source term - the collision operator - which is of algebraic form. Thus this approach offers computational advantages over many other CFD methods, particularly in terms of high performance computing and computing and implementation of boundary conditions.

For these reasons we use the LBM to simulate the interactions between votices and slip boundaries as a dipole is propelled towards a wall in a bounded domain at Reynolds numbers and slip lengths not previously accessed to better understand vortex dynamics and bounded turbulence with slip. The slip length is increased from the near no-slip limit until the free slip condition is reached. We first consider the case of the dipole being released normally towards the wall, and then at oblique release angles to further the understanding of vortex rebounds and energy dissipating structures. We use a two relaxation-time lattice Boltzmann equation (TRT-LBE) model to improve numerical stability[29–31]. Boundary conditions are implemented using the moment-based approach since for straight boundaries aligned with grid points it is known that it satisfies hydrodynamic constraints precisely, with no numerical artifacts[6,32–36] and has been shown to be well-suited for slip velocity boundary conditions, which can be implemented locally at grid points[37].

We note briefly that the LBM has received a lot of attention for its application to microfluidics in the slip-flow regime (see Reis and Dellar[37] for an overview) but most (although by no means all) of these studies are either restricted to relatively simple flows (planar channels or one-dimensional velocity profiles) or suffer from numerical affects due to the boundary condition implementation. Although such flows are not under investigation here, the robustness of the numerical method discussed in this article and the reliability of the results gives evidence that the moment-based boundary conditions can be utilised in a wider variety of flows that exhibit slip. Furthermore, the LBM has been recently used as a numerical tool to study near wall turbulence with a partial slip condition to satisfy a skin friction requirement[38] and turbulent flow interacting with porous media[39], as might be found on modern aerofoils to reduce noise. While distinct from the objectives and flow under study here, they highlight the importance and the capabilities of the LBM to study turbulence

and wall effects.

After a discussion of the key features of the lattice Boltzmann method this article follows Sutherland[16,17] by studying the behaviour of the dipole wall collision in a square box, but using a TRT-LBM with moment-based boundary conditions for implementing the Navier-slip condition. Note that since there is no data is provided in the benchmark article we compare the general behaviour of the dissipation of the kinetic energy, total enstrophy, maximum velocity, trajectory of the dipole and vorticity plots. Our method is verified against the benchmark data and shown to be very accurate with second order spatial convergence. We then extend the study to dipole-wall collisions in a box with slip lengths and Reynolds numbers not previously studied. Our numerical experiments reveal new physics of the dipole-wall collision problem with no-slip and slip walls at an angle of $45°$. The primary dipole that rebounds from the corner of the domain induces new dipoles and this emanation is stopped by the decay of the primary vortex. The 'rolling mill effect' of producing a regular succession of dipoles in some cases is similar to that observed for normal dipole-wall collisions. Furthermore, the mathematical relationship between the dissipation of the kinetic energy and the total enstrophy is discussed and we show that in the presence of wall slip an additional dissipation term contributes to this relationship.

II. THE TWO RELAXATION TIME DISCRETE BOLTZMANN EQUATION

The lattice Boltzmann equation can be derived from the discrete velocity Boltzmann equation (DBE). In terms of microscopic velocities $\mathbf{c}_j$, see Figure 1, the discrete Boltzmann equation with a two-relaxation-time (TRT) collision operator can be written as[40,41]

$$\partial_t f_j + \mathbf{c}_j \cdot \nabla f_j = -\frac{1}{\tau^+}\left(\frac{1}{2}(f_j + f_{\widehat{j}}) - f_j^{(0+)}\right) \\ -\frac{1}{\tau^-}\left(\frac{1}{2}(f_j - f_{\widehat{j}}) - f_j^{(0-)}\right), \qquad (1)$$

where f_j is the probability distribution function for particles with velocity $\mathbf{c}_j$ and $\widehat{j}$ is the opposite direction to j so that $\mathbf{c}_{\widehat{j}} = -\mathbf{c}_j$. In this work we consider the D2Q9 velocity set, as shown in Figure 1. The left hand side of equation (1) describes the propagation of f_j. The right side is the collision operator which represents a relaxation process to an equilibrium state for each f_j. In the TRT model, even and odd parts of the velocity distribution function are relaxed at different rates, τ^+ and τ^-, respectively. This will be explained further in Section II A.

The equilibrium functions are also split into even and odd parts,

$$f_j^{(0+)} = w_j \rho \left(1 + \frac{9}{2}(\mathbf{c}_j \cdot \mathbf{u})^2 - \frac{3}{2}\mathbf{u}^2\right), \\ f_j^{(0-)} = 3 w_j \rho (\mathbf{c}_j \cdot \mathbf{u}), \qquad (2)$$

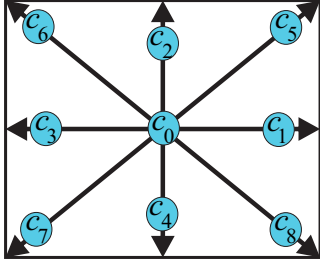FIG. 1: The D2Q9 lattice.

such that

$$f_j^{(0)} = f_j^{(0+)} + f_j^{(0-)}, \tag{3}$$

with weights

$$w_j = \begin{cases} 4/9, & \text{if } j = 0, \\ 1/9, & \text{if } j = 1, \dots, 4, \\ 1/36, & \text{if } j = 5, \dots, 8. \end{cases} \tag{4}$$

The equilibria in equation (2) are functions of the macroscopic density and velocity, which are defined through the first two moments of f_j (see equation (5)). The third moment is the momentum flux tensor, $\mathbf{\Pi}$. The first three moments of f_j define

$$\rho = \sum_j f_j; \quad \rho\mathbf{u} = \sum_j f_j\mathbf{c}_j; \quad \mathbf{\Pi} = \sum_j f_j\mathbf{c}_j\mathbf{c}_j \tag{5}$$

If we take the first three moments of equation (1), apply a Chapman-Enskog expansion, and consider only terms up to leading order in relaxation times, we can show that embedded within the discrete velocity Boltzmann equation are the weakly compressible Navier-Stokes equations[32,35,42]

$$\partial_t \rho + \nabla \cdot \rho\mathbf{u} = 0; \tag{6}$$
$$\partial_t \rho\mathbf{u} + \nabla \cdot (\mathbf{\Pi}^{(0)} + \tau^+ \mathbf{\Pi}^{(1)}) = 0; \tag{7}$$

where $\mathbf{\Pi}^{(0)} = \sum_j f_j^{(0)} \mathbf{c}_j\mathbf{c}_j$ is the leading order contribution to

$\mathbf{\Pi}$ and $\mathbf{\Pi}^{(1)}$ is its first correction in the expansion,

$$\mathbf{\Pi}^{(0)} = \frac{\rho}{3}\mathbf{I} + \rho\mathbf{uu}, \tag{8}$$

$$\mathbf{\Pi}^{(1)} = -\frac{\rho}{3}\left(\nabla\mathbf{u} + \left(\nabla\mathbf{u}\right)^T\right) + \mathscr{O}(Ma^3). \tag{9}$$

Here, $Ma \ll 1$ is the Mach number, $\mathbf{I}$ is the identity matrix and the kinematic viscosity is defined to be $\nu = \tau^+/3$.

A. The Two Relaxation Time Lattice Boltzmann Equation

The lattice Boltzmann equation can be found by integrating both sides of equation (1) from t to $t + \Delta t$

$$f_j(\mathbf{x}+\mathbf{c}_j, t+\Delta t) - f_j(\mathbf{x},t) = \int_t^{t+\Delta t}\left[-\frac{1}{\tau^+}\left(\frac{1}{2}(f_j + f_{\hat{\jmath}}) - f_j^{(0+)}\right)\right.$$
$$\left. - \frac{1}{\tau^-}\left(\frac{1}{2}(f_j - f_{\hat{\jmath}}) - f_j^{(0-)}\right)\right]ds. \tag{10}$$

The left side of equation (10) is exact while the right side of equation (10) can be approximated by the trapezoidal rule to yield

$$f_j(\mathbf{x}+\mathbf{c}_j, t+\Delta t) - f_j(\mathbf{x},t) = \frac{\Delta t}{2}[\Omega(\mathbf{x}+\mathbf{c}j, t+\Delta t) + \Omega(\mathbf{x},t)], \tag{11}$$

where Ω is the integrand in equation (10). This is a second order but implicit system of algebraic equations. To transform this implicit system into an explicit algorithm we follow He *et al.*[43] and perform the change of variables

$$\bar{f}_j(\mathbf{x},t) = f_j(\mathbf{x},t) + \frac{\Delta t}{2\tau^+}\left(f_j^+(\mathbf{x},t) - f_j^{(0+)}(\mathbf{x},t)\right)$$
$$+ \frac{\Delta t}{2\tau^-}\left(f_j^-(\mathbf{x},t) - f_j^{(0-)}(\mathbf{x},t)\right) \tag{12}$$

where f_j^+ and f_j^- are the even and odd parts of f_j:

$$f_j^+ = \frac{1}{2}(f_i + f_j), \tag{13}$$

$$f_j^- = \frac{1}{2}(f_i - f_j). \tag{14}$$

The TRT-LBE for $\bar{f}_j$ can be found by substituting equation (12) into equation (11) to yield

$$\bar{f}_j(\mathbf{x}+\mathbf{c}_j, t+\Delta t) = \bar{f}_j(\mathbf{x},t) - \frac{\Delta t}{(\tau^+ + \Delta t/2)}\left[\frac{1}{2}(\bar{f}_j(\mathbf{x},t) + \bar{f}_{\hat{\jmath}}(\mathbf{x},t)) - f_j^{(0+)}(\mathbf{x},t)\right] - \frac{\Delta t}{(\tau^- + \Delta t/2)}\left[\frac{1}{2}(\bar{f}_j(\mathbf{x},t) + \bar{f}_{\hat{\jmath}}(\mathbf{x},t)) - f_j^{(0-)}(\mathbf{x},t)\right]. \tag{15}$$

The even relaxation time is usually set according to the Reynolds number Re, $\tau^+ = 3UH/Re$ where U and H are the characteristic velocity and length. The odd relaxation time is determined from a special parameter named 'the magic parameter' $\Lambda = \tau^+\tau^-$. Λ is chosen judiciously to enhance the numerical stability. In this work we chose $\Lambda = 1/4$, since it is

Moments	Combination of unknowns at south boundary
$\rho, \rho u_y, \Pi_{yy}$	$\bar{f}_2 + \bar{f}_5 + \bar{f}_6$
$\rho u_x, \Pi_{xy}, Q_{xyy}$	$\bar{f}_5 - \bar{f}_6$
$\Pi_{xx}, Q_{xxy}, S_{xxyy}$	$\bar{f}_5 + \bar{f}_6$

TABLE I: Moment combinations for unknown $\bar{f}_i$ at a south boundary.

Moments	Combination of unknowns at east boundary
$\rho, \rho u_x, \Pi_{xx}$	$\bar{f}_3 + \bar{f}_6 + \bar{f}_7$
$\rho u_y, \Pi_{xy}, Q_{xxy}$	$\bar{f}_6 - \bar{f}_7$
$\Pi_{yy}, Q_{xyy}, S_{xxyy}$	$\bar{f}_6 + \bar{f}_7$

TABLE II: Moment combinations for unknown $\bar{f}_i$ at an east boundary.

known to be a numerically favourable value[6,31,40]. Mass and momentum are conserved by collisions so can be obtained directly from $\bar{f}_j$ just as from f_j

$$\rho = \sum_j \bar{f}_j, \qquad (16)$$

$$\rho \mathbf{u} = \sum_j \bar{f}_j \mathbf{c}_j, \qquad (17)$$

while the next moment of $\bar{f}_j$ is not conserved and given by

$$\overline{\mathbf{\Pi}} = \sum_j \bar{f}_j \mathbf{c}_j \mathbf{c}_j = \left(1 + \frac{\Delta t}{2\tau^+}\right) \mathbf{\Pi} - \frac{\Delta t}{2\tau^+} \mathbf{\Pi}^{(0)}, \qquad (18)$$

where $\mathbf{\Pi}^{(0)}$ can be found in equation (8). Thus the momentum flux can be reconstructed simply from

$$\mathbf{\Pi} = \frac{2\tau^+ \overline{\mathbf{\Pi}} + \Delta t \mathbf{\Pi}^{(0)}}{2\tau^+ + \Delta t}. \qquad (19)$$

B. Imposing slip boundary conditions with the moment-based method

For D2Q9 lattice Boltzmann models there are after each streaming step three unknown (incoming) distributions at boundary points (assuming that the boundaries are straight and aligned with grid points). To determine these three unknown functions, the moment-based method imposes boundary conditions on three linearly independent hydrodynamic moments and then solves these equations[33]. We will explain the method for the cases of slip and shear stress-free conditions.

Let's consider first a south boundary for illustration. Here, the slip velocity u_s is assumed to satisfy the Navier-slip boundary condition, which says that the tangential velocity at the wall is proportional to the shear rate at the surface,

$$u_s = \ell_s \frac{\partial u}{\partial y}\bigg|_{wall}, \qquad (20)$$

where ℓ_s refers to the slip length and y is the direction normal to the wall. At the wall, the incoming functions are $\bar{f}_2, \bar{f}_5, \bar{f}_6$. In Table I, the unknown functions can be seen in one of three linear combinations. In this table, Q_{xxy}, Q_{xyy}, and S_{xxyy} are the components of the third and fourth order D2Q9 LBM moments. They are the only remaining moments and they do not appear in the hydrodynamic equations of motion. Only the equilibrium parts of the third order tensor are used in the Chapman–Enskog expansion to obtain the Navier-Stokes equations and the fourth order moment is not used directly. Moments in the same row of Table I are linearly dependent. Thus to find the three unknowns we must use one moment equation from each of the three rows. That is, we impose a boundary condition on one moment from each row in the table to give us three linearly independent equality constraints that can be solved easily for the three unknown $\bar{f}_j$ at the boundary. It is natural to pick the hydrodynamic moments. From Table I, we chose ρu_y from the first row, ρu_x from the second row (because we want to impose velocity boundary conditions) and the tangential stress Π_{xx} from the third row (the only remaining hydrodynamic moment). For the slip boundary, the following three constraints are applied

$$\rho u_y = 0; \quad \rho u_x = \rho u_s; \quad \Pi_{xx} = \Pi_{xx}^{(0)} = \rho/3 + \rho u_s^2. \quad (21)$$

The condition on Π_{xx} follows from the Chapman-Enskog expansion, $\mathbf{\Pi} \simeq \mathbf{\Pi}^{(0)} + \tau^+ \mathbf{\Pi}^{(1)}$, and $\mathbf{\Pi}^{(1)} \propto \nabla \mathbf{u} + \nabla \mathbf{u}^T$. The equilibrium part is $\Pi_{xx}^{(0)} = \frac{\rho}{3} + \rho u_s^2$ and the viscous stress $\Pi_{xx}^{(1)} = 2\rho \partial_x u_x$ is found from equation (9). In this work it is assumed that $\Pi_{xx}^{(1)}$ is small compared to $\Pi_{xx}^{(0)}$ at the wall (and this has been confirmed numerically) so that $\partial_x u_x \approx 0$ and thus the condition can be stated as $\Pi_{xx} = \Pi_{xx}^{(0)}$. Following Reis and Della[37], the gradient $(\partial u/\partial y)$ that is necessary for the slip condition defined by (20) is calculated from the shear stress moment Π_{xy} and known distributions at the boundary. From the Chapman-Enskog expansion, $\Pi_{xy} \simeq \Pi_{xy}^{(0)} + \tau^+ \Pi_{xy}^{(1)}$ at the wall. The contribution at equilibrium is $\Pi_{xy}^{(0)} = \rho u_x u_y = 0$ and $\Pi_{xy}^{(1)}$ can be found from equation (9), which says that $\Pi_{xy}^{(1)} \propto \partial_y u_x$ and $\partial_x u_y = 0$. Therefore $\Pi_{xy} = -\mu \partial u_x/\partial y$ and the slip velocity is $u_s = -(\ell_s/\mu)\Pi_{xy}$.

Since our algorithm is in terms of the transformed variables $\bar{f}_j$ not f_j, the boundary conditions must be translated into constraints on "barred" quantities[37]:

$$\rho \bar{u}_y = 0,$$

$$\rho \bar{u}_s = -\frac{3\zeta H}{\rho(2\tau^+ + 1)}\overline{\Pi}_{xy}, \qquad (22)$$

$$\overline{\Pi}_{xx} = \frac{\rho}{3} + \rho u_s^2.$$

where ζ is the dimensionless slip length and the width H in the discrete system is $H = H_n = (N_{lb} - 1)\Delta x$, where N_{lb} is the number of grid points in a characteristic length and Δx is the grid spacing. Note that the slip length in equation (20) can be expressed in terms of the dimensionless ζ: $\zeta = \ell_s/H$. Solving equation (22) gives the three unknown distribution functions

$\bar{f}_2, \bar{f}_5, \bar{f}_6$ in terms of known ones

$$\bar{f}_2 = \bar{f}_1 + \bar{f}_3 + \bar{f}_4 + 2(\bar{f}_7 + \bar{f}_8) - \frac{\rho}{3} - \rho \bar{u}_s^2,$$

$$\bar{f}_5 = \frac{\rho}{6} - \bar{f}_1 - \bar{f}_8 + \rho \bar{u}_s(\bar{u}_s + 1)/2, \qquad (23)$$

$$\bar{f}_6 = \frac{\rho}{6} - \bar{f}_3 - \bar{f}_7 + \rho \bar{u}_s(\bar{u}_s - 1)/2.$$

where the density ρ at the boundary is calculated from using the fact that the vertical velocity is zero at the wall: $\rho = \bar{f}_0 + \bar{f}_1 + \bar{f}_3 + 2(\bar{f}_4 + \bar{f}_7 + \bar{f}_8)$. The shear stress in terms of $\bar{f}_i$ can be found from equation (18) as follows:

$$\overline{\Pi}_{xy} = \sum_j \bar{f}_j c_{jx} c_{jy} = \Pi_{xy} + \frac{\Delta t}{2\tau}\left(\Pi_{xy} - \Pi_{xy}^{(0)}\right). \qquad (24)$$

Thus the slip velocity at the wall can be found from the shear stress (24) and the known distribution functions of equation (23)[37]:

$$\bar{u}_s = -\frac{6\zeta H(-\bar{f}_1 + \bar{f}_3 + 2(\bar{f}_7 - \bar{f}_8))}{\rho(2\tau + 1 + 6\zeta H)}. \qquad (25)$$

For stress-free boundaries, different moments should be chosen. The implementation of this case will be given for the east wall as an example, see Table II. The hydrodynamic condition that was imposed for free-slip wall at the east wall is $\partial u_y/\partial x = 0$. This derivative is embedded within the off-diagonal component of the second-order moment of the LBM,

$$\Pi_{xy} = \sum_j f_j c_{jx} c_{jy} \approx \Pi_{xy}^{(0)} + \tau^+ \Pi_{xy}^{(1)}$$

$$= \rho u_x u_y - \frac{\tau^+}{3}\left(\frac{\partial u_x}{\partial y} + \frac{\partial u_y}{\partial x}\right). \qquad (26)$$

Thus, to impose the free slip condition, $\Pi_{xy} = 0$ must be set, since the component of the velocity normal to a wall and its derivative at the wall are zero. In Table II instead of using the moment ρu_y from the second row we will pick Π_{xy}. So the conditions will be:

$$\rho u_x = 0; \quad \Pi_{xy} = 0; \quad \Pi_{yy} = \Pi_{yy}^{(0)}, \qquad (27)$$

where $\Pi_{yy}^{(0)} = \frac{\rho}{3} + \rho u_y^2$ is found from equations (8). In terms of barred conditions, this conveniently translates to $\overline{\Pi}_{xy} = 0$ and $\overline{\Pi}_{yy} = \overline{\Pi}_{yy}^{(0)}$, by using equation (19). Solving the conditions of equation (27) for $\bar{f}_j$ yields the incoming distributions

$$\bar{f}_3 = \bar{f}_1 + \bar{f}_2 + \bar{f}_4 + 2(\bar{f}_5 + \bar{f}_8) - \frac{\rho}{3} - \rho u_y^2,$$

$$\bar{f}_6 = \frac{\rho}{6} - \bar{f}_2/2 - \bar{f}_4/2 - \bar{f}_8 + \rho u_y^2/2, \qquad (28)$$

$$\bar{f}_7 = \frac{\rho}{6} - \bar{f}_2/2 - \bar{f}_4/2 - \bar{f}_5 + \rho u_y^2/2.$$

The density and momentum can be obtained from known functions and imposed conditions: $\rho = \bar{f}_0 + \bar{f}_2 + \bar{f}_4 + 2(\bar{f}_1 + \bar{f}_5 + 2\bar{f}_8)$, $\rho \bar{u}_y = -\overline{\Pi}_{xy} + \bar{f}_2 - \bar{f}_4 + 2\bar{f}_5 - 2\bar{f}_8$.

For both slip and shear stress-free conditions, five constraints are needed to find five unknown distribution functions at the corners. In this flow no-slip boundary conditions will be used at the intersecting walls[32,44]. We note that although the moment-based approach can be used to satisfy hydrodynamic boundary conditions precisely and locally at grid points and has been shown to assist highly accurate computations when used with TRT schemes, it is (at present at least) limited to straight boundaries placed on nodes.

III. DIPOLE-WALL COLLISION

The dipole wall collision flow is simulated using the TRT-LBE described previously. The flow is in the domain $D = \{\mathbf{x} \in R^2 | -1 \le x \le 1, -1 \le y \le 1\}$. The initial numerical setup follows[1] where the characteristic velocity is given by $U = \frac{1}{4}\int\int |\mathbf{u}|^2 dx dy = 1$. The Reynolds number is defined in terms of the half width H of the domain as $Re = UH/\nu$. The vorticity distribution of the monopoles is obtained from

$$\omega_0 = \omega_e(1 - (r/r_0)^2)\exp(-(r/r_0)^2). \qquad (29)$$

The two primary monopoles are placed in the centre of the domain at location (x_1, y_1) and (x_2, y_2). The initial position of the two cores of vorticity are given according to the angle of incidence. From equation (29), the initial velocity distribution for the two monopoles are given by

$$u_{x0} = -\frac{1}{2}|w_e|(y - y_1)\exp\left(-(r_1/r_0)^2\right) \qquad (30)$$

$$+ \frac{1}{2}|w_e|(y - y_2)\exp\left(-(r_2/r_0)^2\right), \qquad (31)$$

$$u_{y0} = \frac{1}{2}|w_e|(x - x_1)\exp\left(-(r_1/r_0)^2\right) \qquad (32)$$

$$- \frac{1}{2}|w_e|(x - x_2)\exp\left(-(r_2/r_0)^2\right), \qquad (33)$$

where $r_1 = \sqrt{(x - x_1)^2 + (y - y_1)^2}$ and $r_2 = \sqrt{(x - x_2)^2 + (y - y_2)^2}$. The radius of the two cores of the vorticity is set to be $r_0 = 0.1$ and the strength of the vortices $w_e = 299.5$. The development of the total kinetic energy and the enstrophy are the cornerstone to understand the physics of this flow. They are defined respectively as

$$E(t) = \frac{1}{2}\int_{-1}^1 \int_{-1}^1 |\mathbf{u}^2|(\mathbf{x}, t) dx dy, \qquad (34)$$

$$\Omega(t) = \frac{1}{2}\int_{-1}^1 \int_{-1}^1 |\omega^2|(\mathbf{x}, t) dx dy, \qquad (35)$$

where the vorticity is given by $\omega = \partial_x u_y - \partial_y u_x$. The above setup yields $E(0) = 2$ and $\Omega(0) \approx 800$. For non-symmetrical wall-dipole collisions with respect to the centre of the square box, the angular momentum is calculated as

$$L(t) = \int_{-1}^1 \int_{-1}^1 (xu_y(\mathbf{x}, t) - yu_x(\mathbf{x}, t)) dx dy. \qquad (36)$$

Re	N_{lb}(normal)	N_{lb}(oblique)30°	N_{lb}(oblique)45°
625	513	513	513
1250	769	769	769
2500	1025	1025	769
5000	3073	4097	1537

TABLE III: The minimum resolution for convergence for dipole wall collision with no-slip walls.

Various grid resolutions N_{lb} are used to examine the convergence of the TRT-LBE. The convergence study for this work is based on the previous study of dipole wall collision with no-slip boundaries in Mohammed *et al.*[6], see Table III. However, at large slip lengths for $Re \geq 5000$ the simulations needed less refined grids to converge than for the no-slip case, because the wall velocity gradient is smaller for slip conditions than for no-slip and the near-wall flow is thus more easily resolved.

A. Normal dipole slip collision

We implement a normal dipole wall collision with slip boundary conditions. The two monopoles of the dipole are initially centred at $(x_1, y_1) = (0, 0.1)$ and $(x_2, y_2) = (0, -0.1)$. The slip length will be taken between 0.002 and 1 which is the half channel width and thus approaching free-slip. The Reynolds numbers will be between $625 \leq Re \leq 10000$.

1. Effects of slip length

As an initial validation, we compared results for Re = 1252 with those obtained by Sutherland[16,17], whose computations were performed for only this single Reynolds number. The results compared very well qualitatively, indicating similar patterns of behaviour. As slip length increased, general decreases were observed for energy dissipation, maximum enstrophy and the number of enstrophy peaks as well as predicted increases in maximum wall velocities. Sharp increases in dissipation corresponded exactly to peaks in enstrophy. Detailed comparisons also showed very good levels of agreement in peak values of enstrophy and wall velocity for slip lengths between 0.002 and 0.02. Corresponding peaks for smaller slip lengths were smaller than those obtained by[16] but we note that peak enstrophy values in particular for no-slip and very small slip lengths agree very well with those reported by[1] so we are justified in having confidence in our computations.

Initially, two counter-rotating vortices move towards the east wall and subsequently collide with it. Figure 2 shows the behaviour of the dipole after it has collided with the wall. The contour levels for the figures are identical for all vorticity plots in this work. The vortices that are then generated at the wall combine and create dipoles that rebound from the wall to induce additional dipoles. The generation of these dipoles depends on the conditions of the wall. In the case of slip boundaries and compared with the no-slip case[6], the number of dipole rebounds from the boundary decreases and
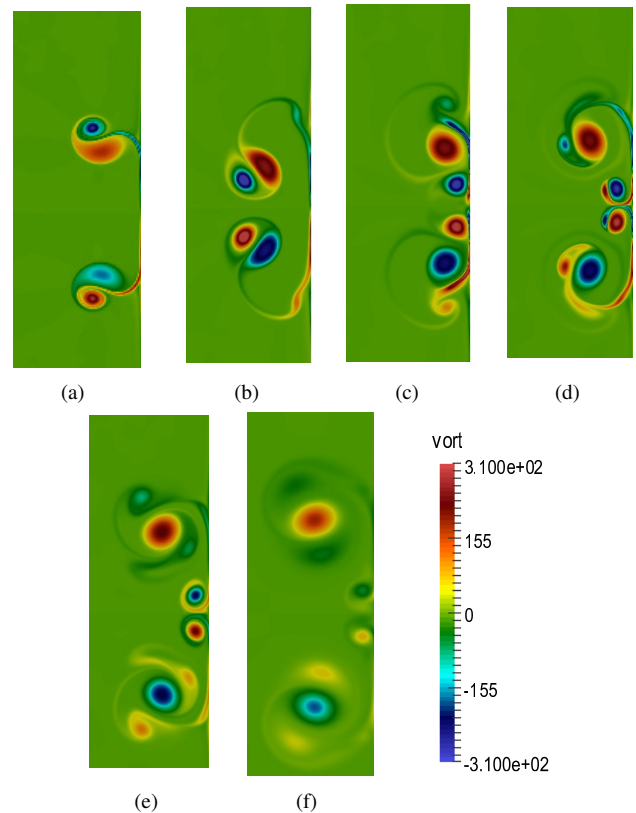

(a) (b) (c) (d)

(e) (f)

vort

FIG. 2: Plots of vorticity for normal wall dipole collision at $Re = 2500$ and $\zeta = 0.002$. Contours are shown in the subdomain $0.5 \leq x \leq 1$, $-0.6 \leq y \leq 0.8$ in the vicinity of the collision at times: (a) $t = 0.4$, (b) $t = 0.5$, (c) $t = 0.6$, (d) $t = 0.7$, (e) $t = 1$ and (f) $t = 1.8$.

fewer vortices are generated from the boundary. The dynamics of the collision with a slip wall are less complicated than for the no-slip collision.

For $Re = 2500$ and slip length $\zeta = 0.002$ around $t = 0.4$ a dipole collides with the slip wall and is forced to rebound by the impact of the secondary core of vortices similar to the no-slip case. After $t = 0.5$ the secondary monopoles join together at the centre of the wall and create a secondary dipole that sticks to and rotates at the wall, as shown in Figure 2 (b). This behaviour differs from the 'rolling mill' observed in no-slip case where the secondary dipole has the strength to travel further from the wall generating a regular succession of dipoles[1,6]. A vorticity filament that separates from the boundary layer surrounds the secondary monopoles at around $t = 0.7$. The dipole continues to rotate near the wall until around $t = 1.8$ then the primary dipole starts to lose strength. No additional dipoles detach from the boundary layer other than the primary and secondary ones after the second dipole wall collision.

To understand the effect of larger slip length on the behaviour of the dipole, the flow with slip length $\zeta = 0.01$ is studied. Figure 3 shows only the top half of the domain, since the normal collision is symmetric about the horizontal centreline. Until the beginning of the second collision around $t = 0.5$, the flow features are similar to those for smaller slip lengths.
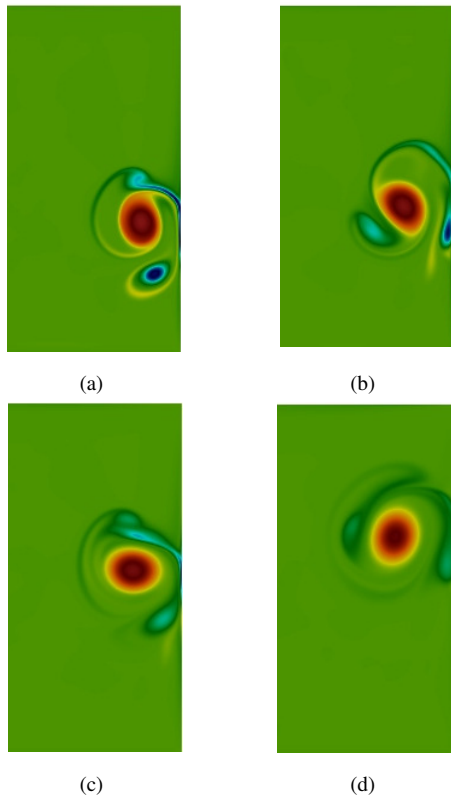
FIG. 3: Plots of vorticity for normal wall dipole collision for $Re = 2500$ and $\zeta = 0.01$. Contours are shown in the subdomain $0.5 \leq x \leq 1, 0 \leq y \leq 1$ in the vicinity of the collision at times: (a) $t = 0.5$, (b) $t = 0.6$, (c) $t = 0.7$ and (d) $t = 1$.

FIG. 4: (a) The kinetic energy and (b) total enstrophy for $Re = 2500$ and different slip lengths ζ.

After the second collision, the pair of dipoles splits further because of the slip effect and the secondary monopoles merge with the primary ones at around $t = 0.6$. Simultaneously, a bundle of vortices starts to rotate above the primary dipole which is generated from the filament sheet at the boundary. After $t = 1$, these additional vortices lose their strength while the primary dipole retains its strength and continues moving along the slip wall.

Figure 4 displays the dissipation of total kinetic energy and the total enstrophy at different slip lengths for $Re = 2500$. Comparing our plots with those found in Sutherland[16,17] (who, as noted above performed computations for Re = 1252 only) we see similar general behaviour where the dissipation of total kinetic energy and the total enstrophy follow the same pattern. Since the number of vortex wall collisions decreases when the slip length is increased, the dissipation of the energy decreases as the slip length increases and is highest in the no-slip case. Abrupt changes in dissipation are associated with vorticity generation due to dipole-wall collisions. For different slip lengths, the dissipation of the energy is the same until around $t = 0.3$ where the first collision happens, then it starts to separate according to the slip length. Figure 4(b) demonstrates that the maximum enstrophy decreases with increasing slip length and the peaks are highest for the collision with the no-slip wall. For the highest values of slip length, vorticity generation as the dipole collides with the wall is minimal
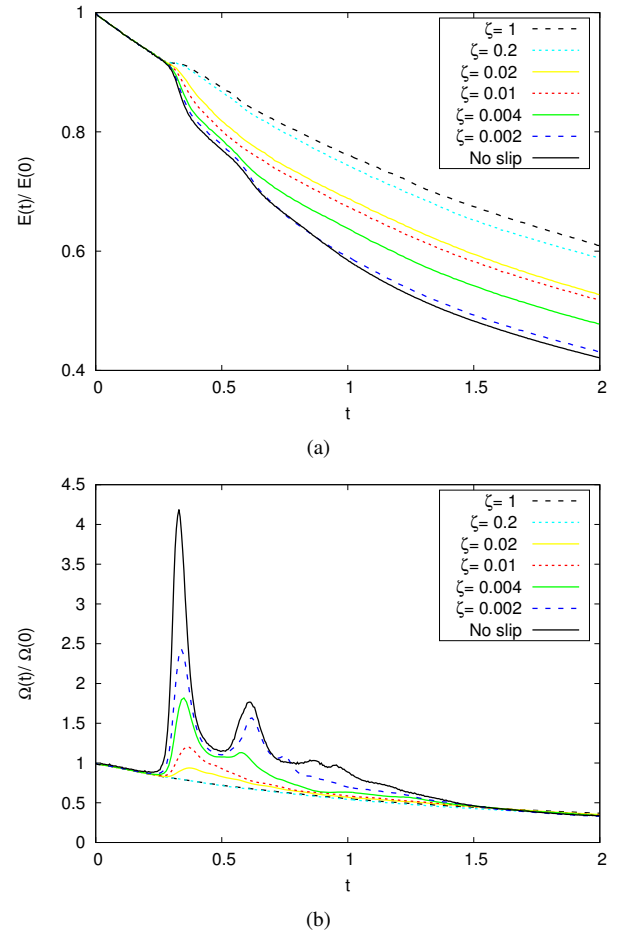
hence the dissipation and enstrophy are essentially unaffected by the presence of the wall.

2. The effect of slip length and Reynolds number on the flow

Figures 5 and 6 give a view of how the Reynolds number affects the generation of vortices. The results show the strength of the secondary dipole at two times for a slip length of $\zeta=0.002$. When $Re < 2500$, the secondary monopoles meet at the centre of the wall and create one dipole without any additional monopoles appearing in the boundary layer. However, for $Re \geq 5000$ the small secondary monopoles continuously move with the primary one without losing their strength. At $t = 0.8$ (Figure 5) a number of small high magnitude vortices appear at the filament sheet that surrounds the primary monopoles. The number of collisions increases with an increase in Reynolds number. Subsequently, the gap between the two primary monopoles increases with Reynolds number. Similar to the collision with the no-slip wall, where Orlandi[2] described the behaviour of the secondary dipole at high Reynolds numbers for no-slip collision, the secondary dipole at the slip boundary is smaller in size and higher in
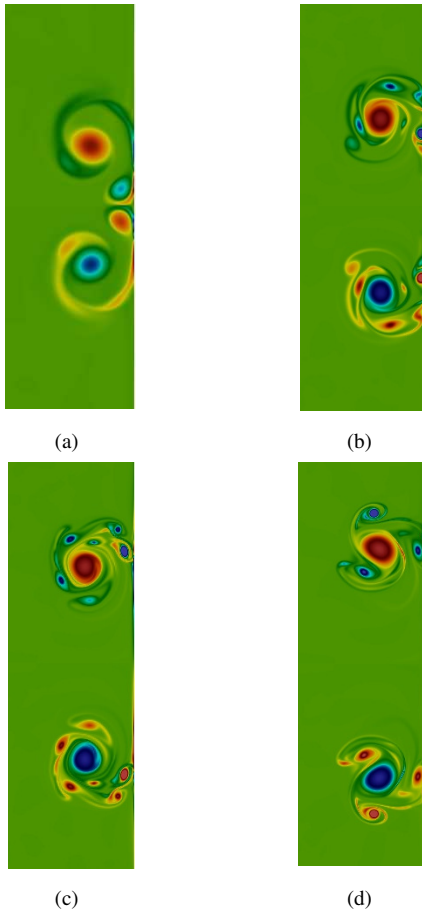
FIG. 5: Plots of vorticity for normal wall dipole collision with $\zeta = 0.002$ at $t = 0.8$ for various Reynolds numbers. Contours are shown in the subdomain $0.5 \leq x \leq 1, -0.8 \leq y \leq 0.8$ in the vicinity of the collision. (a) $Re = 1252$, (b) $Re = 5000$, (c) $Re = 7500$ and (d) $Re = 10000$.
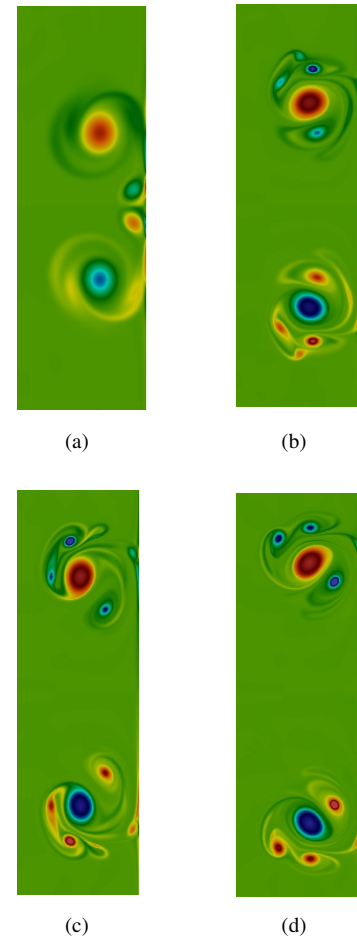

FIG. 6: Plots of vorticity for normal wall dipole collision at $\zeta = 0.002$ and $t = 1$ for various Reynolds numbers. Contours are shown in the subdomain $0.5 \leq x \leq 1, -0.8 \leq y \leq 0.8$ in the vicinity of the collision. (a) $Re = 1252$, (b) $Re = 5000$, (c) $Re = 7500$ and (d) $Re = 10000$.

strength than was the case for smaller Reynolds numbers. That is because at higher Reynolds numbers, the dissipation of the small secondary vortex is slower. Moreover, increasing the slip length reduces the rolling-mill effect (i.e. the continual generation of new dipoles) observed for no-slip conditions[35] especially for high Reynolds numbers since the space between the two primary monopoles is increased.

To demonstrate the effect of Reynolds number on the wall with higher slip lengths, Figures 7 and 8 show the influence of Reynolds number on the formulation of vortices at the wall for $\zeta = 0.01$ at times $t = 0.6$ and $t = 1$, respectively. For increasing Reynolds number, the space between the two primary monopoles increases until they reach the top and bottom walls for $Re \geq 5000$. In general, for $Re < 2500$ the small secondary monopoles move towards the primary one, then lose their strength over time. For $Re \geq 5000$ the primary monopoles travel far from each other while the secondary small but high intensity vorticity cores move towards the centre of the wall. For $Re = 7500$ and $Re = 10000$, the two small secondary monopoles that move towards the centre of the wall are enveloped by one high strength vortex.

For different slip lengths and similar to the no-slip case[6],

when the Reynolds number was increased, the dissipation of the energy decreased, as seen by comparing Figure 4(a) and Figure 9(a). The results in Table IV show the impact of the slip and no-slip cases on the dissipation of the kinetic energy for various Reynolds numbers at $t = 2$. In Table V, non-normalized results of the first and second enstrophy maxima are shown for various Reynolds numbers at different slip lengths. Except for $\zeta = 0.01$, one maximum has appeared in the table. The two maximum peaks of the enstrophy increase with higher Reynolds numbers. Also for slip lengths $\zeta > 0$, the enstrophy decreases to around the same value after $t = 1.2$ for $Re \leq 2500$ and after $t = 1.5$ at higher Reynolds numbers. This change coincides with the lack of vorticity formation at the boundary at this period of time, except for the no-slip conditions where the boundary layer is active and continuously induces more vortices.

The maximum slip velocity at the east wall is presented for various Reynolds numbers in Figure 10. Unsurprisingly, the slip velocity at the wall increases with increasing slip. The slip velocity also increases with Reynolds number, consistent with a reduction in boundary layer thickness.
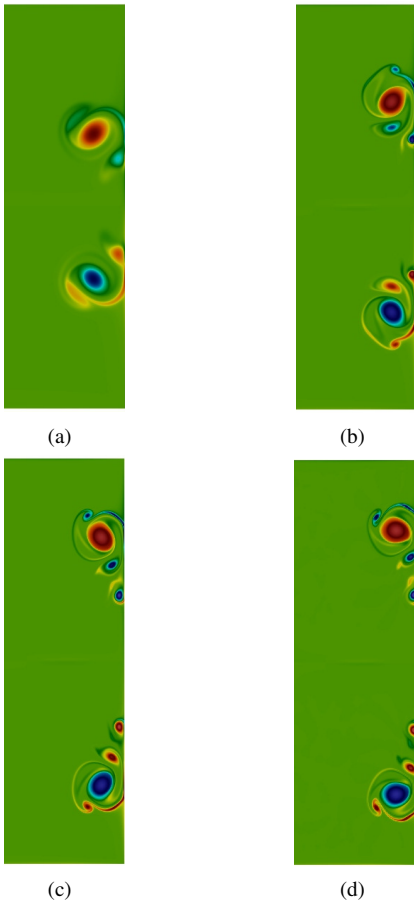
FIG. 7: Plots of vorticity for normal wall dipole collision with $\zeta = 0.01$ at $t = 0.6$ for various Reynolds numbers. Contours are shown in the subdomain $0.4 \leq x \leq 1, -1 \leq y \leq 1$ in the vicinity of the collision. (a) $Re = 1252$, (b) $Re = 5000$, (c) $Re = 7500$ and (d) $Re = 10000$.

FIG. 8: Plots of vorticity for normal wall dipole collision with $\zeta = 0.01$ at $t = 1$ for various Reynolds numbers. Contours are shown in the subdomain $0.4 \leq x \leq 1, -1 \leq y \leq 1$ in the vicinity of the collision. (a) $Re = 1252$, (b) $Re = 5000$, (c) $Re = 7500$ and (d) $Re = 10000$.

	Re				
ζ	1252	2500	5000	7500	10000
0.02	0.344	0.562	0.742	0.76	0.808
0.01	0.333	0.517	0.678	0.753	0.875
0.002	0.272	0.430	0.620	0.699	0.739
0	0.606	0.419	0.554	0.642	0.645

TABLE IV: The kinetic energy at $t = 2$, $E(2)/E(0)$, for normal dipole wall collision for different Reynolds numbers and slip lengths.

Re	ζ	t_1	$\Omega(t_1)$	t_2	$\Omega(t_2)$
	0.01	0.36	9520	-	-
2500	0.002	0.34	1945	0.64	1153
	No slip	0.32	3305	0.61	1413
	0.01	0.37	1093	-	-
7500	0.002	0.33	2705	0.58	2017
	No slip	0.32	7626	0.60	5013
	0.01	0.37	1109	-	-
10000	0.002	0.33	2897	0.57	2207
	No slip	0.32	9519	0.62	6455

TABLE V: First and second maximum enstrophy $\Omega(t)$ of the dipole wall collision by using TRT-LBM. Results are given for different slip lengths and Reynolds numbers.
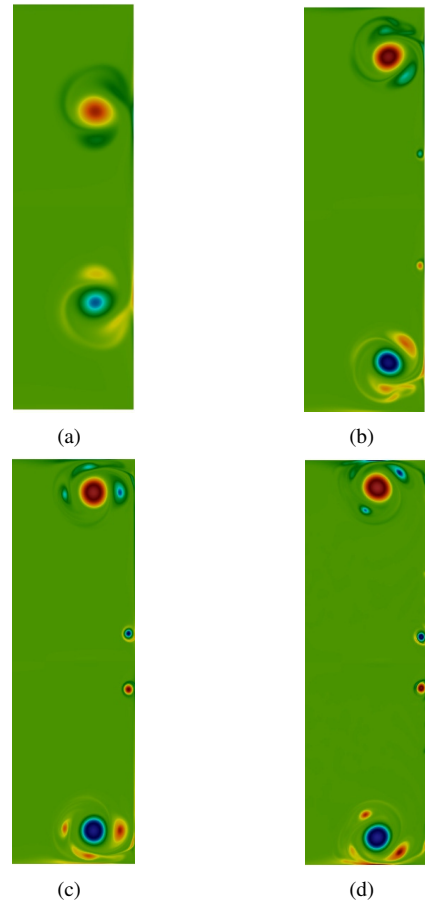
3. Trajectory of the dipole

Kramer[4] made a comparison between the path of a dipole colliding with no-slip and stress-free boundaries at $Re = 1250$. Also the trajectory of a dipole with different slip lengths and stress-free boundaries in a channel for $Re = 1252$ has been studied by Sutherland[16,17]. Following Sutherland[16], we compute the trajectory of the maximum vorticity for a dipole colliding with different types of boundaries. The comparison is given for the path for no-slip, slip and the stress-free walls. Figure 11 describes the trajectory of the maximum vorticity of the positive half of the dipole. This figure traces the trajectory of the dipole at $Re = 2500$ for ζ=0.004, 0.002, 0.01, 0.02, and the no slip collision. Note that the no-slip condition is approached as $\zeta \to 0$. Before the first wall collision, the trajectories overlap for different slip lengths for all Reynolds numbers. After the first wall collision the dipole stays close to the wall for a greater distance for higher slip lengths. For smaller slip lengths, as the number of the collisions increases, the rebounds of the dipole from the wall causes the primary vortex to move as an almost circular trajectory near the wall. For no-slip walls, the trajectory of the dipole appears as a full-
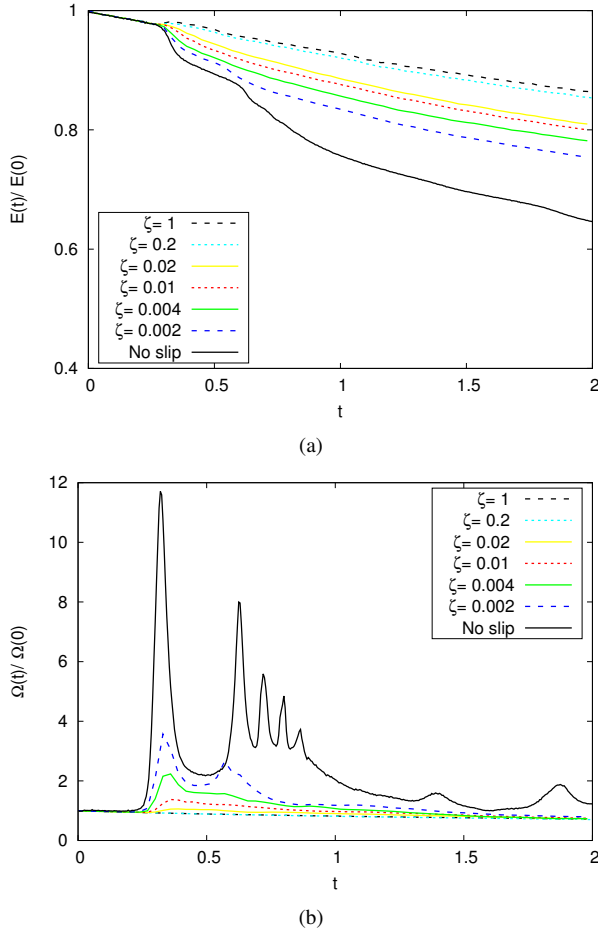
(a)

(b)

FIG. 9: (a) The kinetic energy and (b) total enstrophy for normal dipole wall collisions at $Re = 10000$.

(a)

(b)

FIG. 10: The maximum velocity for the normal wall collision at $x = 1$ with different slip when (a) $Re = 1252$ and (b) $Re = 10000$.

circular shape.

To observe the behaviour of the dipole that collides with a stress-free wall, we applied the moment-based boundary condition with the stress-free constraint from Section II B. Along the stress-free wall, the two primary monopoles separate with the first collision and roll up at the wall. The positive and negative monopoles move with opposite directions without any rebound and do not generate any further vortices at the wall. The walls with slip lengths $\zeta \geq 0.1$ act as a stress-free wall. Figure 12 shows that the trajectory with slip boundary conditions and slip length $\zeta = 0.2$ matches the trajectory computed using stress-free conditions.

IV. OBLIQUE WALL DIPOLE COLLISIONS WITH SLIP BOUNDARIES

In this section we perform a detailed study of the behaviour of dipole collision with various slip lengths at release angle $30°$. Also the physics of a dipole that collides with no-slip and slip walls at an angle of $45°$ will be discussed. At each angle of incidence, the influence of the slip length and the Reynolds number on the collision and the formation of the vortices at
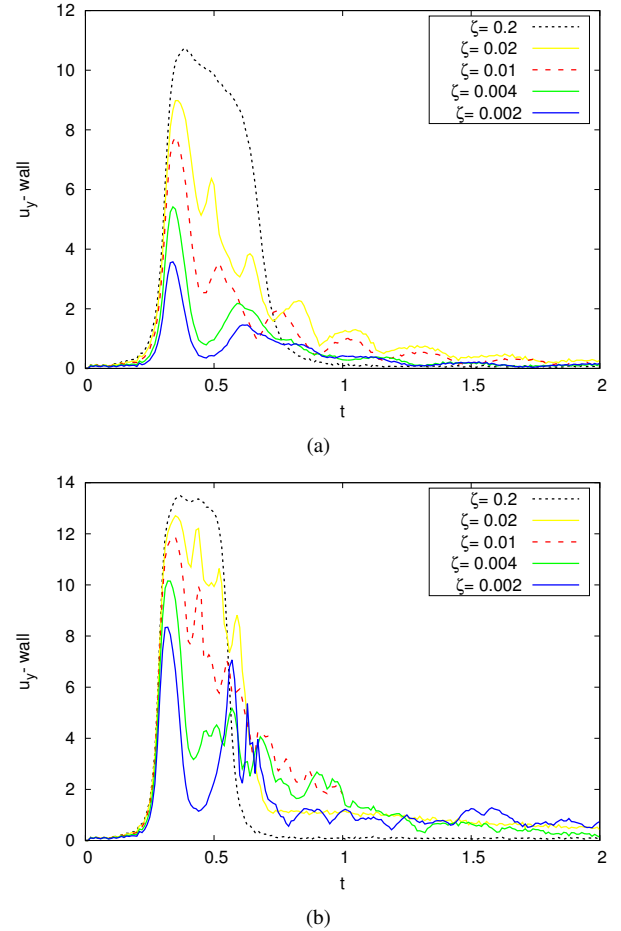
the wall is discussed.

A. Dipole slip wall collision at an angle of $30°$

In this case, the two counter-rotating vortices of the dipole are located initially at (0.0839, 0.0866), (0.1839, -0.0866). Figures 13 and 14 plot the vorticity contours when then dipole is released at an angle of $30°$ with different slip lengths at at times $t = 0.7$ and $t = 1$, respectively. They show that the primary vortex moves up, through the corner and around the wall towards the east slightly more quickly as the slip length increases. For the no-slip dipole wall collision, the secondary vortex moves upwards towards the corner while it rotates downwards for finite values of ζ. It should be mentioned that the primary and secondary vortices interact only for no-slip and small ζ. By looking at the general behaviour of the total energy, enstrophy and the maximum velocity at the wall, the differences between each slip and no-slip case can be observed. Figures 15 and 16 show the dissipation of the energy, the rise of the enstrophy peaks and the maximum velocity at the wall. The energy dissipation rate, the enstrophy peaks and the wall slip velocity are all smaller for the $30°$ case then for
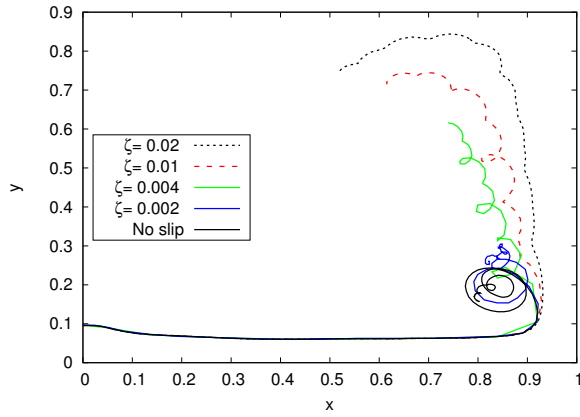
FIG. 11: Trajectory of the maximum vorticity in the top half of the domain in a range of time $t \in [0,2]$ with different slip lengths. The Reynolds number is 2500.
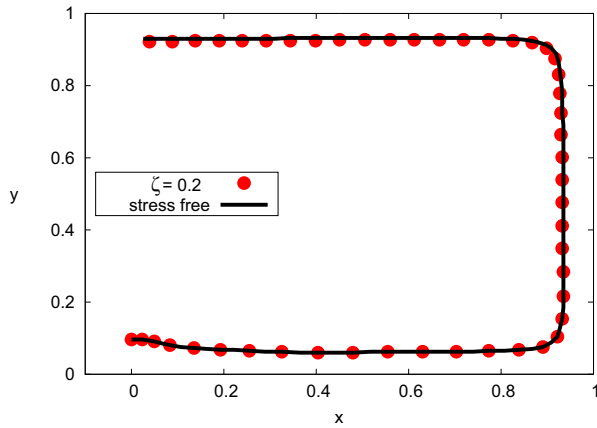

FIG. 12: Trajectory of the maximum vorticity with stress-free boundary conditions and for slip boundary conditions with slip length $\zeta = 0.2$ in the top half of the domain in a range of time $t \in [0,2]$. The Reynolds number is Re=2500.

FIG. 13: Vorticity plots for oblique wall dipole collision at angle of $30°$ and time $t = 0.7$ for no slip walls and for slip-lengths $\zeta = 0.002, 0.01$ when $Re = 2500$. Contours are shown in the subdomain $0.2 \le x \le 1, -0.4 \le y \le 1$ in the vicinity of the collision. (a) No slip, (b) $\zeta = 0.002$ and (c) $\zeta = 0.01$.

FIG. 14: Vorticity plots for oblique wall dipole collision at angle of $30°$ for no slip, slip $\zeta = 0.002, 0.01$ at $t = 1$ and $Re = 2500$. Contours are shown in the subdomain $0.2 \le x \le 1, -0.4 \le y \le 1$ in the vicinity of the collision. (a) No slip, (b) $\zeta = 0.002$ and (c) $\zeta = 0.01$.

the normal collision. Figure 17 accentuates the effect of the Reynolds numbers on the vortex boundary interaction for $\zeta = 0.002$. In Mohammed et al[6], the authors showed that, for no-slip wall conditions, by increasing Re the complexity of the flow increases due to the creation of additional vortices at the wall. However, by applying the slip condition the effect of the Reynolds number is diminished and the boundary induces fewer vortices with larger slip lengths. Moreover, the space between the positive and negative cores increases with the increasing Reynolds numbers when it is compared with the no-slip case.

To obtain all the information about the dipole wall collision at an angle of $30°$ for various slip lengths, the total angular momentum is plotted for $Re = 2500$ and $Re = 7500$ in Figure 18. The plots illustrate that before the first wall interaction, the angular momentum is independent of slip length. After collision, the results for the angular momentum are highly sensitive to the slip length. The recurrence of the fluctuation of the angular momentum decreases for large slip lengths, especially for $\zeta \ge 0.1$. By tracing the vorticity contours for these
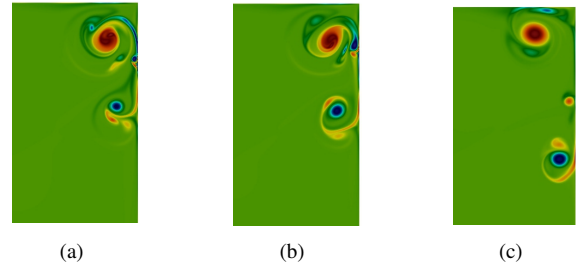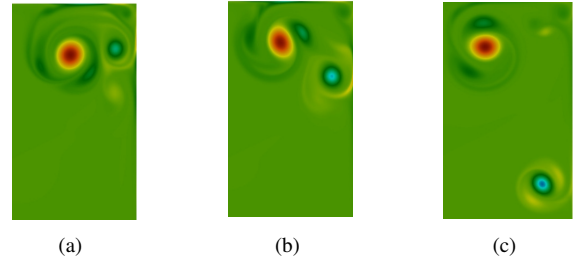
two slip lengths, the two high and low peaks of $L(t)$ can be explained. During the movement of the dipole along the slip wall and when the dipole reaches the corners, the angular momentum has sudden jumps. The high peaks of the angular momentum occur when negative monopoles reach the bottom corners, while the minimum jumps describe the arrival of positive monpoles at the upper corners. For $\zeta = 0.2$, the initial dipole separates into two distinct vortices but no further vortices are created. The relatively large oscillations for this case represent interactions between these two vortices and the corners of the flow domain.

B. Dipole slip wall collision at an angle of $45°$

Numerous authors have discussed the flow when the dipole collides normally with the no-slip walls and at an oblique angle of $30°$, for example[1,5,6]. We consider here collisions at an angle of incidence of $45°$. Before we consider collisions with slip walls, the physics of collisions with no-slip boundaries is explained. At this angle of collision the dipole moves initially from the centre of the box at the position $(-0.0707, 0.0707), (0.0707, -0.0707)$ towards the top right corner. The primary dipole reaches the corner and collides with it around $t = 0.4$ which induces a secondary dipole from the intersecting walls. Thus, the primary dipole produces a new pair of dipoles which follow the secondary one. This process repeats itself and a new 'rolling-mill' creates a succession of dipoles. The new pairs of monopoles reflect from the cor-
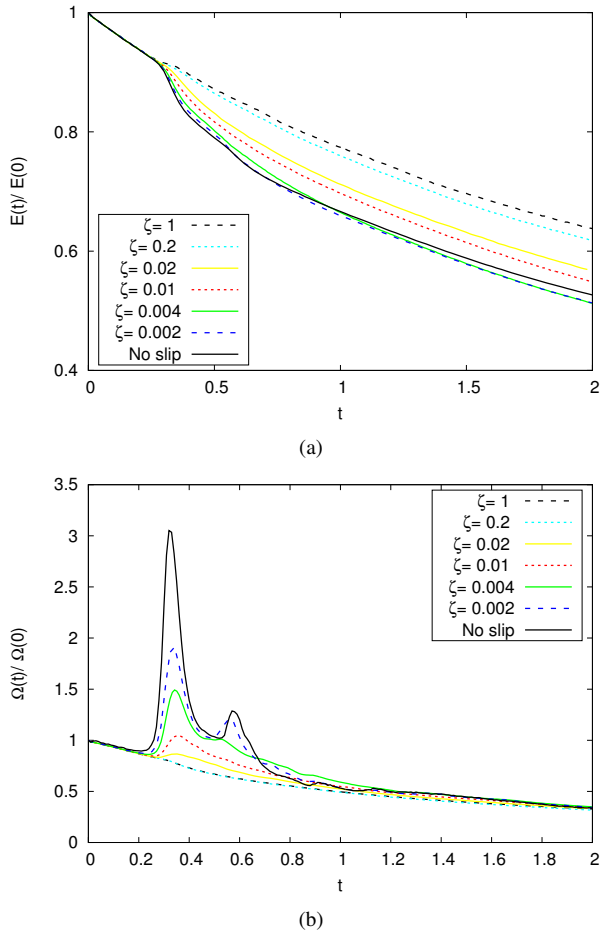
(a)

(b)

FIG. 15: (a) The total kinetic energy and (b) total enstrophy at $Re = 2500$ for oblique dipole-wall collision at an angle of $30°$ for different slip lengths.
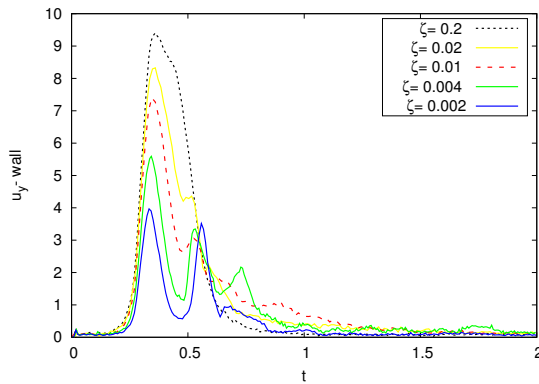

FIG. 16: The maximum velocity at $x = 1$ with different slip for $Re = 2500$ at an angle of $30°$.

(a)

(b)

(c)

FIG. 17: Vorticity fields of dipole wall collision at an angle of $30°$ at time $t = 1.5$ with slip length $\zeta = 0.002$ and (a) Re=2500, (b) Re= 5000 and (c) Re=7500. Contours are shown in the subdomain $0 \leq x \leq 1, 0 \leq y \leq 1$ in the vicinity of the collision.

ner and then move towards the bottom-left corner. Finally, the dipole creation ends due to the dissipation of the primary dipole at the top-right corner. During this process the pairs of additional dipoles lose their strength during their travels. Figure 19 shows a sequence of dipoles generated from the initial di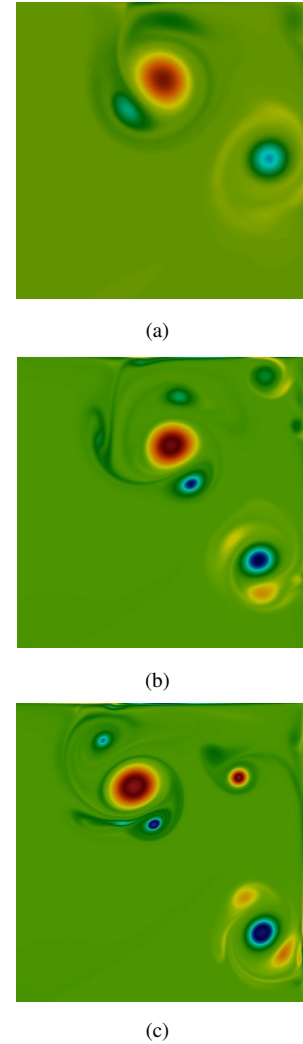pole for $Re = 2500$. Note that the general behaviour of the dipole collision with no-slip wall at an angle of $45°$ for other Reynolds numbers is similar to $Re = 2500$ case. The primary dipole loses its strength over time while the secondary dipoles are bounced towards the opposite corner.

For the collision with a slip boundary, the dissipation of the primary dipole differs from that for the collision with the no-slip wall. Figure 20 displays a comparison between a dipole which collides with slip and no slip boundaries for $Re = 2500$. The data is presented at $t = 0.8$ and $t = 1.2$. By looking at the Figures we can see a new rolling-mill effect only for no-slip or very small slip lengths. For slip lengths larger than 0.002, the primary dipole loses its strength less quickly than for smaller slip lengths. Moreover, the primary and secondary vortices become separated and do not interact with each other to create new dipoles. This leads to a reduction in the number of vortices that are generated at the top corner.

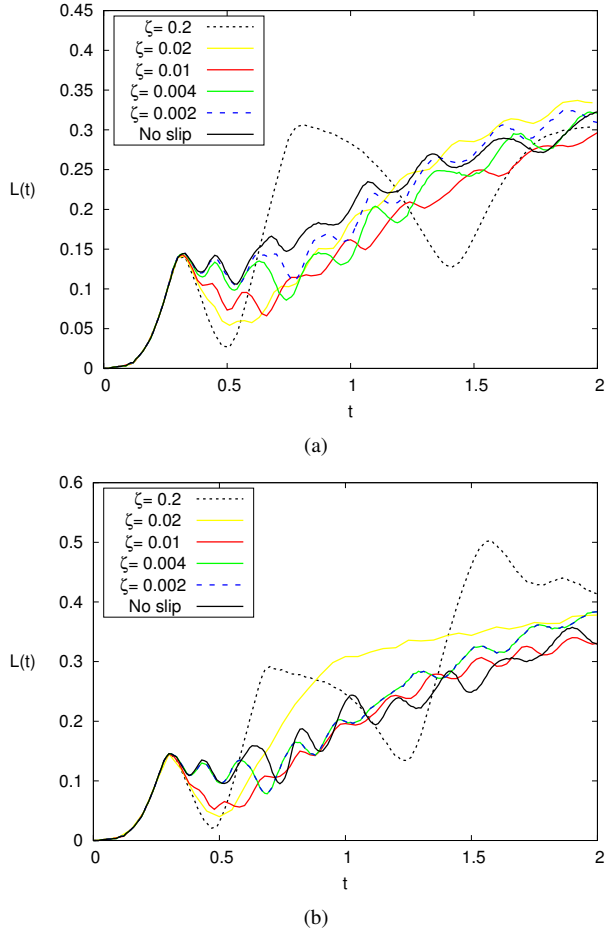Figure 21 shows the total kinetic energy and the total en-

(a)

(b)

FIG. 18: The total angular momentum at (a) Re=2500 and (b) Re=7500 for oblique wall dipole collision at an angle of $30°$ and different slip lengths.

FIG. 19: Vorticity contours of dipole-wall collision at an angle of $45°$ with the no-slip wall when $Re = 2500$. Contours are shown in the subdomain $0 \leq x \leq 1, -0.2 \leq y \leq 1$ in the vicinity of the collision at times: (a) $t = 0.4$, (b) $t = 0.56$, (c) $t = 0.66$ and (d) $t = 1$.

strophy for $Re = 2500$. The dissipation of the energy behaves in an unexpected manner. Here, the dissipation of the energy for $\zeta = 0.002$ is lower than that for no-slip collisions and it is even lower for $\zeta = 0.004$ after $t = 1.0$. However, the enstrophy peaks diminish in magnitude with increasing ζ. This apparent anomaly is explained in Section V.

Figures 22– 24 show that, for $\zeta = 0.004$, by increasing the Reynolds numbers the roll up of the dipole at the corner and the rolling-mill effect diminishes. For a given slip length, increasing Re induces more small dipoles at the corner. For $Re = 5000$, the secondary dipole sticks and rolls up at the corner until its strength reduces at $t = 1$. Meanwhile, what is left from the secondary dipole is an arc of sheets of vortices that surrounds the primary dipole, see Figure 22.

Figure 23 shows that the mechanism of the dipole after collision with the corner for $Re = 7500$ differs from other cases since the dipoles do not detach from the boundary to the opposite direction. Instead, the secondary dipole stimulates a number of small dipoles from the corner that rotate with each other near the corner. At the same time vorticity filament sheets detach from the slip walls which surround the dipoles near the adjoining walls. The two primary monopoles tumble down on the top and right walls, which generates numerous small
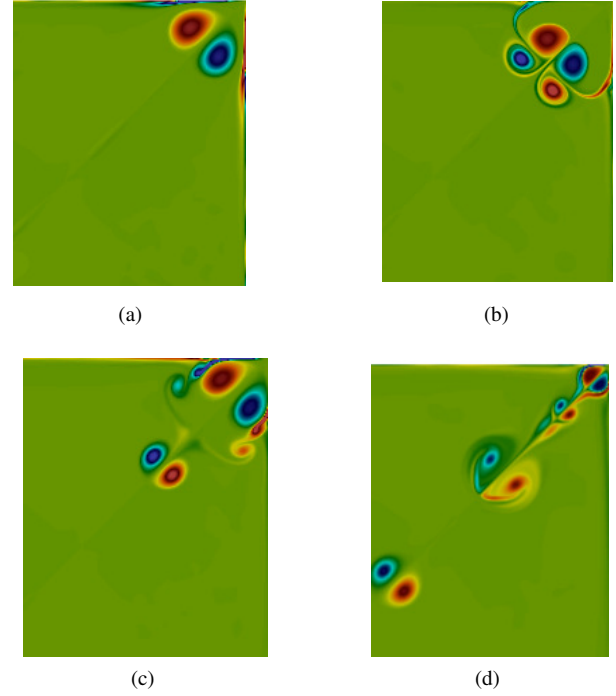
and high strength monopoles that surround the primary dipole and prevent the ejection of further dipoles form the corner. For $Re = 10000$ the vortices at the corner cluster in an orderly manner to produce more dipoles at the corner. The secondary dipole manages to travel alone to the opposite direction leaving the primary dipole in the vicinity of the corner, see Figure 24. In the last two cases, the primary dipole only slowly loses its strength over time.

Table VI summarises the values of the kinetic energy at $t = 2$ to clarify the dissipation of the energy behaviour for different Reynolds numbers and slip lengths for an angle of incidence of $45°$. Firstly, similar to other angles of collision, the dissipation of the kinetic energy decreases by increasing Reynolds numbers for a given slip length. Secondly, in contrast to other angles of collision, the decay of the kinetic energy for the no-slip case is slightly slower than for small slip length, $\zeta = 0.002$, at $t \geq 1.2$ for $Re < 10000$. This confirms the results in Figure 21. For $Re = 10000$, the dissipation rate becomes regular and similar to the ones with normal collision and at an angle of $30°$, where the energy dissipates faster for the no-slip collision. Figure 25 illustrates the dissipation of the kinetic energy and the persistence of the enstrophy for $Re = 10000$ and various slip lengths. For this Reynolds number, the overall dissipation eventually decreases with increasing slip length, in contrast to the behaviour observed for $Re = 2500$ in Figure 21.
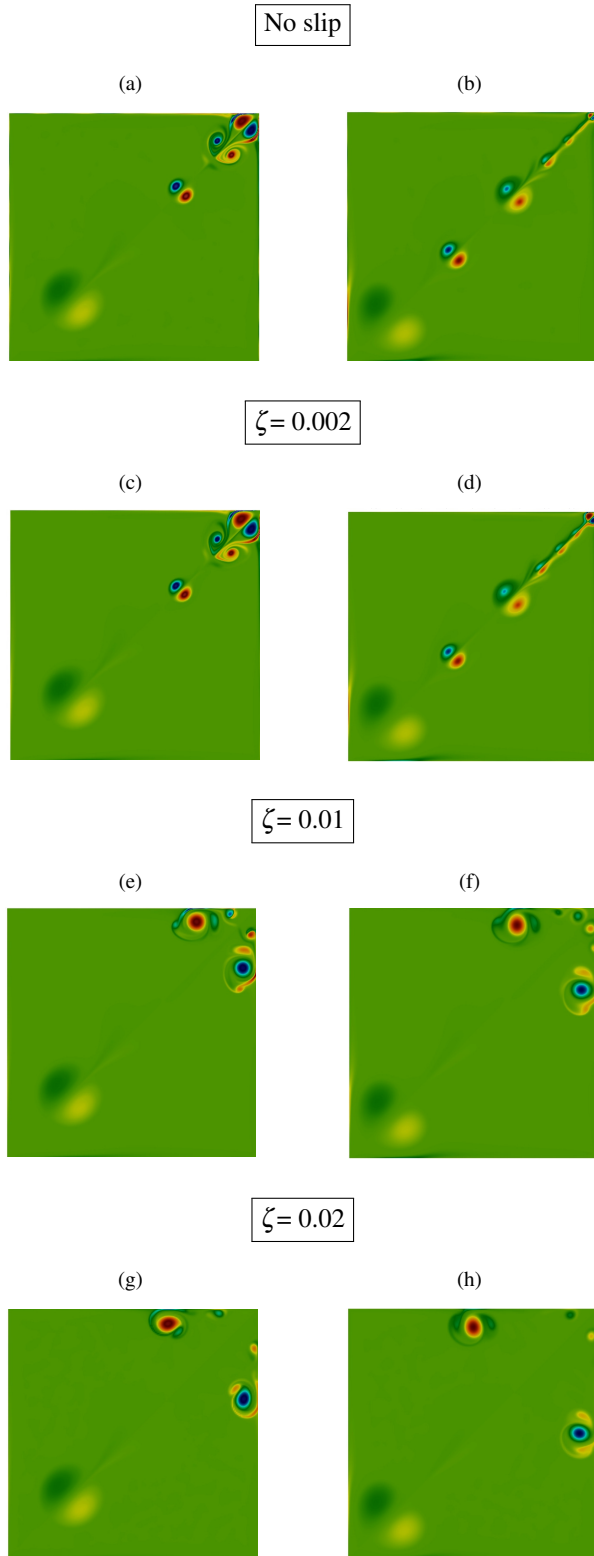
No slip

(a)   (b)

$\zeta = 0.002$

(c)   (d)

$\zeta = 0.01$

(e)   (f)

$\zeta = 0.02$

(g)   (h)

FIG. 20: Vorticity fields of dipole wall collision at an angle of $45°$ and $Re = 2500$ for no slip walls and for slip lengths $\zeta = 0.002, 0.004, 0.01, 0.02$. Note that (a), (c), (e) and (g) are at time $t = 0.8$ while (b), (d), (f) and (h) ar at time $t = 1.2$.
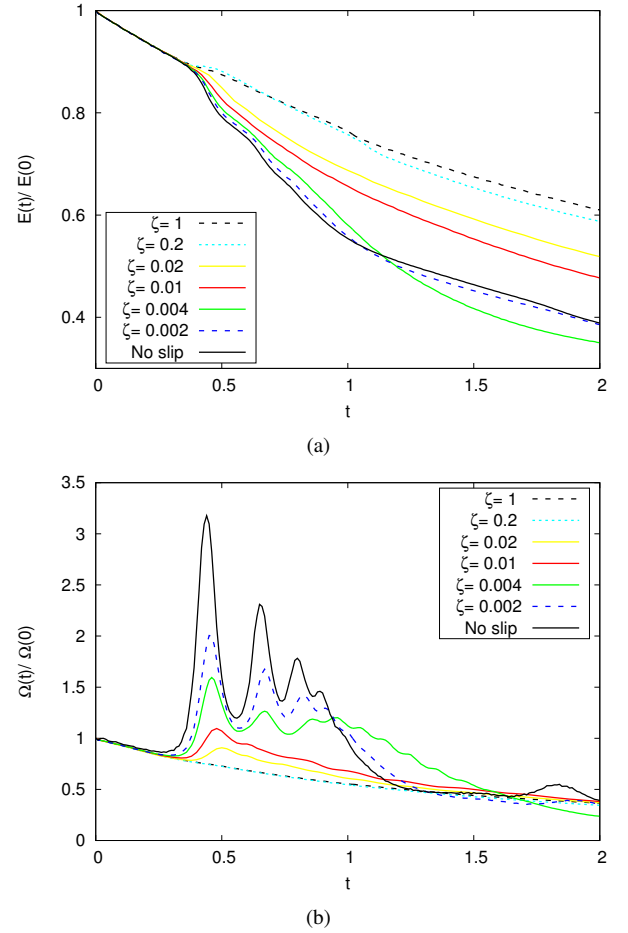

(a)

(b)

FIG. 21: (a) The total kinetic energy and (b) total enstrophy for oblique dipole-wall collisions at an angle of $45°$ when $Re = 2500$ and different slip lengths.

ζ	Re				
	1252	2500	5000	7500	10000
0.02	0.324	0.518	0.690	0.766	0.809
0.01	0.274	0.477	0.661	0.744	0.793
0.002	0.253	0.377	0.504	0.576	0.624
No slip	0.260	0.388	0.519	0.577	0.594

TABLE VI: The kinetic energy at $t = 2$, $E(2)$, for dipole wall collisions at an angle of $45°$ for different Reynolds numbers and slip length.

V. THE RELATIONSHIP BETWEEN THE DISSIPATION OF THE KINETIC ENERGY AND THE ENSTROPHY

For incompressible flow confined within slip walls, the mathematical expression for the relationship between the energy dissipation and the growth of the enstrophy is

$$\frac{d\tilde{E}}{dt} = -\frac{2}{Re}\tilde{\Omega} - \frac{1}{Re}\int_{\tilde{S}}(\tilde{\omega} \times \tilde{\mathbf{u}}) \cdot \mathbf{n} d\tilde{S}. \tag{37}$$

where the overbar indicates a dimensionless quantity. The derivation of equation (37) is given in Appendix A. The second term on the right-hand side of the above equation depends
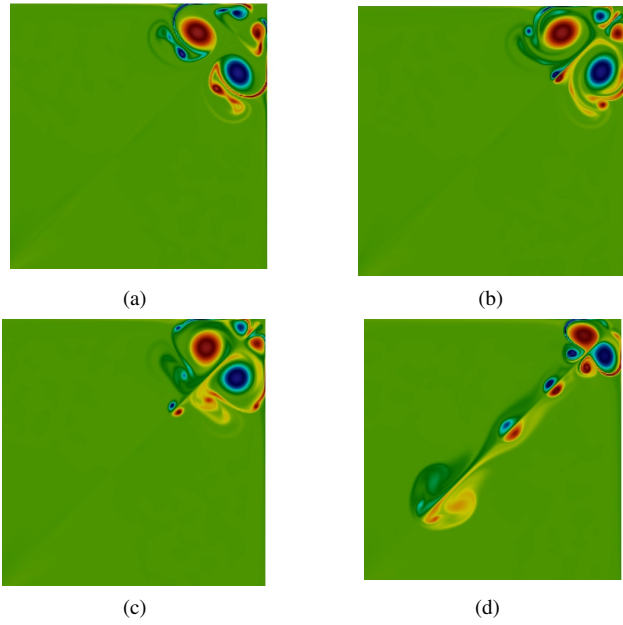
FIG. 22: Vorticity of dipole collision at an angle of 45° with slip length ζ=0.004l and $Re = 5000$. Contours are shown in the subdomain $-0.2 \leq x \leq 1, -0.2 \leq y \leq 1$ in the vicinity of the collision at times (a) $t = 0.7$, (b) $t = 0.8$, (c) $t = 0.9$ and (d) $t = 1.5$.
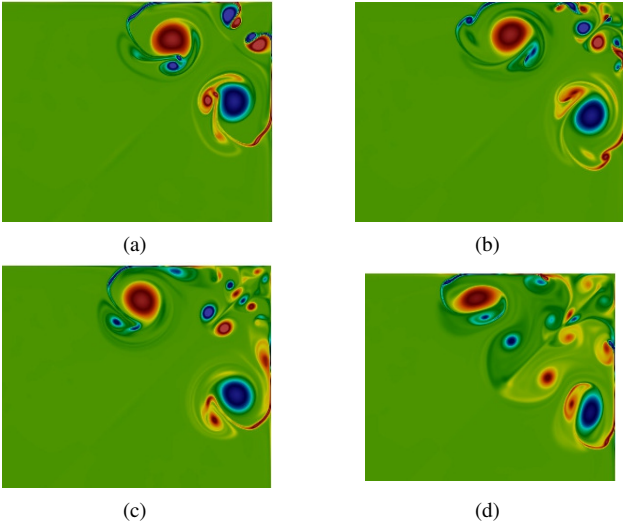

FIG. 24: Vorticity of dipole collision with slip length ζ=0.004 wall at an angle of 45° for $Re = 10000$. Contours are shown in the subdomain $0 \leq x \leq 1, 0 \leq y \leq 1$ in the vicinity of the collision at times (a) $t = 0.7$, (b) $t = 0.9$, (c) $t = 1$ and (d) $t = 1.8$

FIG. 23: Vorticity of dipole-wall collision at an angle of 45° for $Re = 7500$ with the slip length ζ=0.004. Contours are shown in the subdomain $0 \leq x \leq 1, 0.2 \leq y \leq 1$ in the vicinity of the collision at times (a) $t = 0.7$, (b) $t = 0.9$, (c) $t = 1$ and (d) $t = 1.8$.

on the relation between the velocity and the vorticity at the boundary. In fact, equation (37) can explain the increase of the kinetic energy dissipation when the slip length is decreased as in Figure 4(a). By decreasing the slip length, the boundary layer induces more vortices than at higher slip length. Therefore, due to the second term on the right of equation (37), the enstrophy increases, which leads to a more rapid dissipation of the kinetic energy.

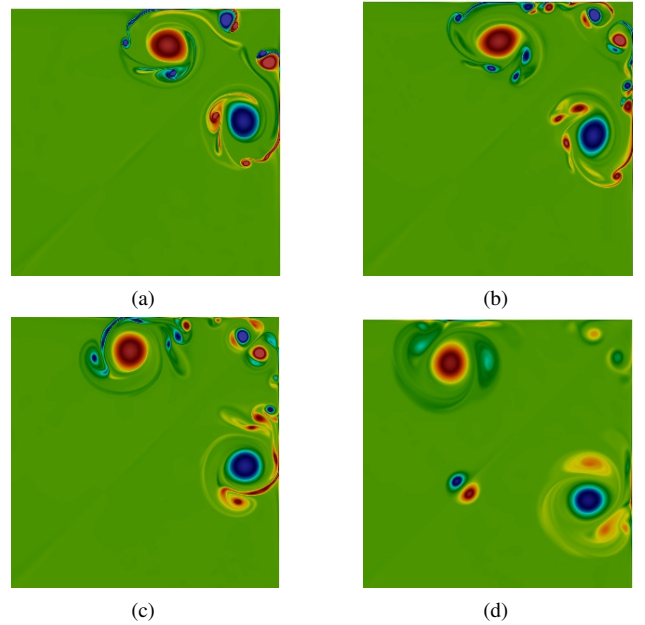For no-slip boundaries, the relation between the kinetic en-

ergy and the enstrophy is

$$\frac{d\tilde{E}}{dt} = -\frac{2}{Re}\tilde{\Omega}. \tag{38}$$

The analysis leading to equation (37) is based upon the assumption that the flow is incompressible. Lattice Boltzmann method simulations are weakly-compressible but compressibility effects can be made smaller by reducing the Mach number in the simulations. Here, we reduce the scaled initial mean velocity $u_{lb} = \frac{1}{(m-1)^2} \int_0^m \int_0^m |\mathbf{u}|^2 dxdy$ in so-called lattice units (computational scale). That amounts to reducing the Mach number from $Ma = 0.01\sqrt{3}$ to $0.001\sqrt{3}$. Reducing the Mach number and using the mean average dissipation over 100 time steps results in a smooth curve and excellent agreement between the two sides of equation (37), as shown in Figure 26. This Figure illustrates the role of the last term in equation (37) for $Re = 2500$ and $Ma = 0.001\sqrt{3}$. This term causes a significant amount of additional, wall-generated dissipation. As discussed below this term contributes significantly to the overall dissipation and must be taken into account for flows with slip. The kinetic energy and the enstrophy which are the focus of previous sections are not significantly affected by random variations. Thus reducing the Mach number as above does not affect the results obtained previously.

To show the effect of extra dissipation due to wall slip, the ratio between the right-hand side of equation (37) and equation (38) is calculated as follows:

$$\vartheta = \frac{max\left|-\frac{2}{Re}\tilde{\Omega} - \frac{1}{Re}\int_{\tilde{S}}(\tilde{\omega} \times \tilde{\mathbf{u}}) \cdot \mathbf{n}d\tilde{S}\right|}{max\left|-\frac{2}{Re}\tilde{\Omega}\right|}. \tag{39}$$
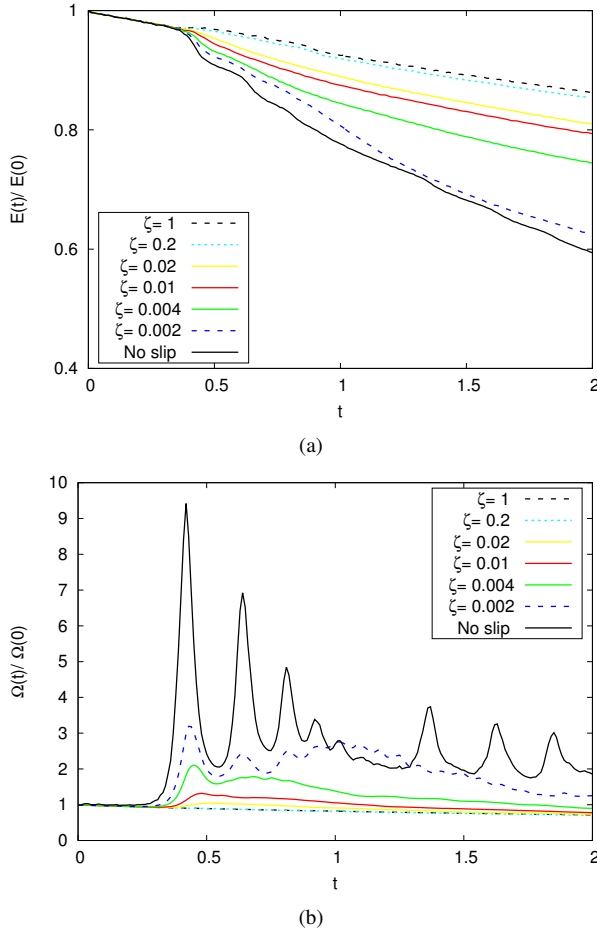
(a)

(b)

FIG. 25: (a) The total kinetic energy and (b) total enstrophy at $Re = 10000$ for oblique dipole-wall collisions at an angle of $45°$ and different slip lengths.
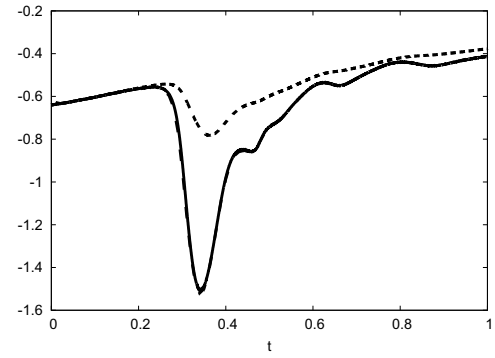

FIG. 26: Relationship between the energy dissipation and the enstrophy in equation (37) for dipole wall collision with slip length $\zeta = 0.004$ and $Re = 2500$. Shown are the left side of the equation (37) (dashed line), the right side (solid line) and the right side of equation (38) (dotted line).
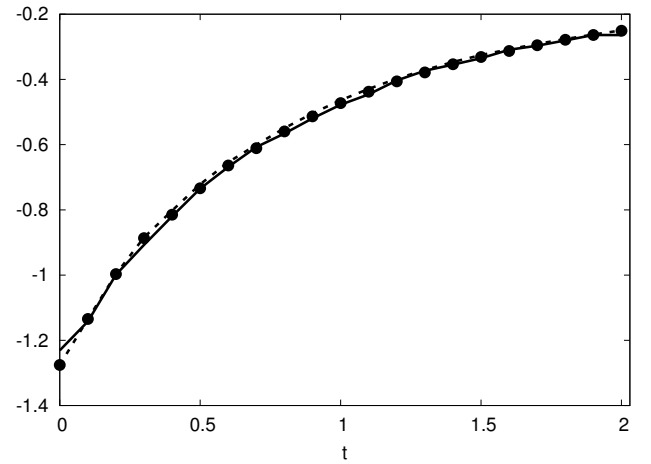

FIG. 27: The relationship between the energy dissipation and the enstrophy in equation (37) for dipole wall collision and $\zeta = 2$ for $Re = 1252$ and $Ma = 0.001\sqrt{3}$. Shown are the left hand side of equation (37) (line), the right hand side (circle) and the right hand side of equation (38) (dotted) .

For no-slip walls, this ratio is unity since the extra dissipation is absent in this case. Table VII and Table VIII show that for a given Re, the ratio first increases as the slip velocity increases with ζ, reaching a maximum value when ζ is between 0.01 and 0.02. In the most extreme case, more than half of the maximum dissipation is due to the wall terms. The ratio then decreases to unity as ζ increases further to the free-slip case. This is because the boundary layer is not present for the shear stress-free boundaries that come from the higher slip lengths, so the effect of the wall term in equation (37) is weak. Figure 27 demonstrates the results for higher slip length $\zeta = 1$ and $Re = 2500$, as an example.

VI. CONCLUSION

We have studied the problem of a dipole colliding with boundaries that permit slip using the lattice Boltzmann method. The Navier-slip condition was imposed locally using a moment-based implementation of hydrodynamic boundary condition. Comparisons with benchmark data for different Reynolds numbers, slip lengths, and collision angles are in ex-

cellent agreement and show second order spatial convergence. The same accuracy is shown for our new implementation of the stress-free conditions.

Previous work showed the generation of secondary dipoles as the primary dipole collided with the wall, and subsequent generation of higher-order dipoles as these interacted with the wall. Individual dipole-wall collisions were associated with sharp enstrophy peaks and increased dissipation. We have highlighted the different physical behaviour of the flow when no-slip is replaced with slip conditions when the dipole collision is normal to the wall. The main feature is the reduced number of higher-order dipoles created as slip increases and hence the slip decreases the magnitude of the enstrophy peaks and reduces the dissipation of energy. For collision angles of $30°$ and small slip lengths the frequency and amplitude of oscillations in time of the angular momentum decreased with an increase in slip lengths. For larger slip lengths we observed a general increase in angular momentum and decrease in oscillatory behaviour, with some high amplitude and low fre-

ζ	t	$Re = 625$	t	$Re = 1250$	t	$Re = 2500$	t	$Re = 5000$
0.0005	0.369	1.061	0.342	1.105	0.324	1.187	0.322	1.275
0.002	0.371	1.201	0.340	1.377	0.329	1.550	0.326	1.750
0.004	0.371	1.343	0.345	1.575	0.329	1.622	0.321	2.165
0.01	0.378	1.524	0.352	1.779	0.329	2.041	0.325	2.224
0.02	0.399	1.545	0.347	1.737	0.340	1.903	0.336	2.061
0.1	0.357	1.162	0.368	1.275	0.355	1.307	0.360	1.317

TABLE VII: The ratio in equation (39) for normal dipole wall collision for different Reynolds numbers and slip lengths.

ζ	t	$Re = 625$	t	$Re = 1250$	t	$Re = 2500$	t	$Re = 5000$
0.0005	0.356	1.052	0.336	1.095	0.322	1.158	0.317	1.255
0.002	0.356	1.177	0.338	1.304	0.325	1.467	0.321	1.696
0.004	0.351	1.279	0.343	1.457	0.330	1.661	0.325	1.905
0.01	0.364	1.408	0.342	1.620	0.337	1.798	0.329	2.004
0.02	0.356	1.374	0.353	1.576	0.342	1.689	0.335	1.790
0.1	0.350	1.126	0.345	1.191	0.342	1.216	0.335	1.220

TABLE VIII: The ratio in equation (39) for $30°$ dipole wall collision for different Reynolds numbers and slip lengths.

quency oscillatory behaviour when the slip length is increased further. The two peaks observed in the angular momentum for collision angles of $30°$ and slip length of 0.2 appear when the two monopoles reach the corners of the domain.

For the $45°$ dipole-wall collision with no-slip or small slip lengths, a new dipole is generated when the initial dipole collides with the corner of the domain. This new dipole the rebounds from the corner, itself producing new dipoles. This behavior repeats, producing a "rolling mill" effect similar to that observed for the normal collisions. However, when the slip length is increased, the dipole separates into two monopoles - the distance between them increasing with slip length – and the magnitude of vorticity is maintained for longer. Primary and secondary vortices do not interact, leading to a reduction in the number and strength of vortices generated by wall collisions. This behavior is similar to that observed in the other cases we studied.

For both normal and $30°$ collisions, higher dissipation is associated with higher maximum enstrophy, both of which increase as slip length decreases. For the $45°$ collision for moderate Re with (dimensionless) slip length 0.004, however, dissipation of energy is higher than for no-slip, whilst the maximum enstrophy was less than that observed for the no-slip case. This apparent anomaly is confirmed with a new theoretical relationship between energy dissipation and enstrophy for incompressible fluids in the presence of slip. This includes a contribution related to wall values of slip velocity and vorticity which reduces to zero for no-slip and free-slip cases but whose value cannot be neglected for finite slip lengths.

We have noted above that we observed the rolling mill effect for both normal and $45°$ impacts. This could be important and destructive in practice if the rate of generation of vortices matched the natural frequencies of structures, and could also a source of noise. Future lines of investigation could include different impact angles to see how sensitive the rolling mill effect is to departures from these angles (thereby destroying symmetry). Furthermore, we have found that wall slip introduces an extra dissipation term in the relationship between

kinetic energy and enstrophy and in some circumstances this can lead to greater dissipation with partial slip boundaries than with no-slip walls. Thus, it is possible that efforts at reducing drag from skin friction (or reducing noice) with effective slip on boundaries[10–14,39] may require some 'tuning' of parameters to avoid unexpected energy losses or noise generation. But such possible implications are in need of further investigation.

Appendix A: Derivation of energy decay equation with wall slip

The decay of the energy after the first collision in a bounded domain can be explained by finding the relation between the dissipation of the total kinetic energy and the production of the vortices at the boundary. The dimensionless relationship can be found from the incompressible Navier-Stokes equations

$$\frac{\partial \mathbf{u}}{\partial t} + \mathbf{u} \cdot \nabla \mathbf{u} = -\frac{1}{\rho}\nabla P + v\nabla^2 \mathbf{u},$$
$$\nabla \cdot \mathbf{u} = 0. \tag{A1}$$

Using the standard identity for the viscous term $\nabla^2 \mathbf{u} = \nabla(\nabla \cdot \mathbf{u}) - \nabla \times \left(\nabla \times \mathbf{u} \right)$ and then multiplying the momentum equation by $\mathbf{u}$ gives,

$$\rho \mathbf{u} \cdot \frac{\partial \mathbf{u}}{\partial t} + \rho \mathbf{u} \cdot \left(\mathbf{u} \cdot \nabla \mathbf{u} \right) = -\mathbf{u} \cdot \nabla P - \mu \mathbf{u} \cdot \left(\nabla \times \left(\nabla \times \mathbf{u} \right) \right). \tag{A2}$$

The first term of equation (A2) represents the dissipation of the kinetic energy per unit volume and by assuming the density ρ is constant we can say that

$$\rho \mathbf{u} \cdot \frac{\partial \mathbf{u}}{\partial t} = \frac{1}{2}\frac{\partial}{\partial t}(\rho |\mathbf{u}|^2) = \frac{\partial E_v}{\partial t}, \tag{A3}$$

where E_v is the energy per unit volume.

Since $\mathbf{u} \cdot \nabla \mathbf{u} = \frac{1}{2} \nabla |\mathbf{u}|^2 + (\nabla \times \mathbf{u}) \times \mathbf{u}$,

$$\mathbf{u} \cdot (\mathbf{u} \cdot \nabla \mathbf{u}) = \frac{1}{2} \mathbf{u} \cdot \nabla |\mathbf{u}|^2 + \mathbf{u} \cdot ((\nabla \times \mathbf{u}) \times \mathbf{u}). \quad (A4)$$

Furthermore,

$$\nabla \cdot \left(|\mathbf{u}|^2 \mathbf{u} \right) = \mathbf{u} \cdot \nabla \left(|\mathbf{u}|^2 \right) + |\mathbf{u}|^2 \nabla \cdot \mathbf{u}. \quad (A5)$$

The pressure term in equation(A2) can be written as

$$\nabla \cdot \left(P\mathbf{u} \right) = P\nabla \cdot \mathbf{u} + \nabla P \cdot \mathbf{u}, \quad (A6)$$

The fourth term of equation (A2) can be rewritten as follows

$$\mathbf{u} \cdot \left(\nabla \times \left(\nabla \times \mathbf{u} \right) \right) = \nabla \cdot \left(\left(\nabla \times \mathbf{u} \right) \times \mathbf{u} \right) + |\nabla \times \mathbf{u}|^2. \quad (A7)$$

Substituting equations (A3), (A5), (A6) and (A7) into equation (A2) gives

$$\frac{\partial E_v}{\partial t} + \nabla \cdot \left((P + E_v)\rho\mathbf{u} + \mu(\boldsymbol{\omega} \times \mathbf{u}) \right) = -\mu |\boldsymbol{\omega}|^2, \quad (A8)$$

where $\boldsymbol{\omega} = \nabla \times \mathbf{u}$ is the vorticity of the flow.

In order to find the total kinetic energy and total enstrophy, both sides of equation (A8) are integrated over domain V

$$\int_V \left(\frac{\partial E_v}{\partial t} + \nabla \cdot \left((P + E_v)\mathbf{u} + \mu(\boldsymbol{\omega} \times \mathbf{u}) \right) \right) dV \quad (A9)$$

$$= -\mu \int_V |\boldsymbol{\omega}|^2 dV. \quad (A10)$$

The first term of the left side of equation (A10) represents the dissipation of the total kinetic energy

$$\int_V \frac{\partial E_v}{\partial t} dV = \frac{dE}{dt}, \quad (A11)$$

while the integration of the right side gives the total enstrophy part

$$-\mu \int_V |\boldsymbol{\omega}|^2 dV = -2\mu\Omega. \quad (A12)$$

What remains is the integration of the second part of equation (A10). Therefore, using the divergence theorem $\int_V \nabla \cdot \mathbf{A} dV = \int_S (\mathbf{A} \cdot \mathbf{n}) dS$ where $\int_S$ is the integration on the boundary and $\mathbf{n}$ is unit normal on it, gives

$$\int_V \nabla \cdot \left((P + E_v)\mathbf{u} + \mu(\omega \times \mathbf{u}) \right) dV \quad (A13)$$

$$= \int_S \left(\left((P + E_v)\mathbf{u} + \mu(\omega \times \mathbf{u}) \right) \cdot \mathbf{n} \right) dS. \quad (A14)$$

Note that the first term of the right side of equation (A14) is cancelled because the fluid velocity is tangential to the wall (so $\mathbf{u} \cdot \mathbf{n} = 0$) normal to the wall. Finally, the link between the dissipation of the kinetic energy and the enstrophy can be represented by

$$\frac{d\tilde{E}}{dt} = -\frac{2}{Re}\tilde{\Omega} - \frac{1}{Re} \int_{\tilde{S}} (\tilde{\omega} \times \tilde{\mathbf{u}}) \cdot \mathbf{n} d\tilde{S}, \quad (A15)$$

where the tiled quantities are the non-dimensional parts of the total kinetic energy, vorticity, velocity and the total enstrophy .

[1] H. Clercx and C.-H. Bruneau, "The normal and oblique collision of a dipole with a no-slip boundary," Comput. Fluids **35**, 245–279 (2006).

[2] P. Orlandi, "Vortex dipole rebound from a wall," Phys. Fluids A: Fluid Dynamics (1989-1993) **2**, 1429–1436 (1990).

[3] H. Clercx and G. van Heijst, "Dissipation of kinetic energy in two-dimensional bounded flows," Phys. Rev. E **65**, 066305 (2002).

[4] W. Kramer, *Dispersion of tracers in two-dimensional bounded turbulence*, Ph.D. thesis, Eindhoven University of Technology, Eindhoven, Netherlands (2007).

[5] J. Latt and B. Chopard, "A benchmark case for lattice Boltzmann: turbulent dipole-wall collision," Int. J. Mod. Phys. C **18**, 619–626 (2007).

[6] S. Mohammed, D. Graham, and T. Reis, "Assessing moment-based boundary conditions for the lattice Boltzmann equation: A study of dipole-wall collisions," Computers and Fluids 176C , 79–96 (2018).

[7] S. J. Barker and S. C. Crow, "The motion of two-dimensional vortex pairs in a ground effect," J. Fluid Mech. **82**, 659–671 (1977).

[8] P. Saffman, "The approach of a vortex pair to a plane surface in inviscid fluid," J. Fluid Mech. **92**, 497–503 (1979).

[9] C. Navier, "Mémoire sur les lois du mouvement des fluides," Mém. Acad. Sci. Inst. F. **6**, 389–440 (1823).

[10] C. Fairhall and R. García-Mayoral, "Spectral analysis of the slip-length model for turbulence over textured superhydrophobic surfaces," Flow, Turbulence and Combustion **100**, 961–978 (2018).

[11] W. Jäger and A. Mikelić, "Couette flows over a rough boundary and drag reduction," Communications in Mathematical Physics **232**, 429–455 (2003).

[12] M. Rastan, S. Foshat, and S. Sekhavat, "High-Reynolds number flow around coated symmetrical hydrofoil: effect of streamwise slip on drag force and vortex structures," J. Marine Sci. Tech. **24**, 500–511 (2019).

[13] C. T. Fairhall, N. Abderrahaman-Elena, and R. García-Mayoral, "The effect of slip and surface texture on turbulence over superhydrophobic surfaces," Journal of Fluid Mechanics **861**, 88–118 (2019).

[14] J. Ibrahim, G. Gomez-de Segura, and R. García-Mayoral, "A unified approach to the study of turbulence over smooth and drag–reducing surfaces," in *11th International Symposium on Turbulence and Shear Flow Phenomena,* (2019).

[15] M. Farge, K. Schneider, *et al.*, "Energy dissipating structures produced by walls in two-dimensional flows at vanishing viscosity," Phys. Rev. Lett. **106**, 184502 (2011).

[16] D. Sutherland, *Numerical study of vortex generation in bounded flows with no-slip and partial slip boundary conditions*, Ph.D. thesis, University of Sydney (2014).

[17] D. Sutherland, C. Macaskill, and D. Dritschel, "The effect of slip length on vortex rebound from a rigid boundary," Phys. Fluids (1994-present) **25**, 093104 (2013).

[18] B. Jamart and J. Nihoul, *Mesoscale/Synoptic Coherent Structures in Geophysical Turbulence*, Vol. 50 (Elsevier, New York,, 1989).

[19] T. von Larcher and P. D. Williams, *Modeling Atmospheric and Oceanic Flows: Insights from Laboratory Experiments and Numerical Simulations*, Vol. 205 (John Wiley & Sons, Hoboken, New Jersey, 2014).

[20] S.-S. Chen, C.-Y. Chow, and M. S. Uberoi, "Effect of slip boundary condition on flow computation in the presence of rotational body forces," Comput. Fluids. **9**, 389–393 (1981).

[21] B. Fiedler, "Axisymmetric tornado simulations with a semi-slip boundary," Fluids **2**, 68–77 (2017).

[22] G. Carnevale, O. Velasco Fuentes, and P. Orlandi, "Inviscid dipole-vortex rebound from a wall or coast," J. Fluid Mech. **351**, 75–103 (1997).

[23] M. Lighthill, "On sound generated aerodynamically," Phil. Trans. R. Soc. A **564**, 1952 (1954).

[24] N. Curle, "The influence of solid boundaries upon aerodynamic sound," Proc. R. Soc. Lond. A **231**, 505–514 (1955).

[25] M. Howe, *Theory of vortex sound*, Vol. 33 (Cambridge University Press, UK, 2003).

[26] Y. Nakashima and O. Inoue, "Sound generation by a vortex ring collision with a wall," Phys. Fluids **20**, 126104 (2008).

[27] X. He and L. Luo, "A priori derivation of the lattice Boltzmann equation," Phys. Rev. E **55**, R6333 (1997).

[28] X. Shan, X. Yuan, and H. Chen, "Kinetic theory representation of hydrodynamics: a way beyond the Navier–Stokes equation," J. Fluid Mech. **550**, 413–441 (2006).

[29] I. Ginzburg, "Lattice Boltzmann modeling with discontinuous collision components: Hydrodynamic and advection-diffusion equations," J. Stat. Phys. **126**, 157–206 (2007).

[30] I. Ginzburg, "Equilibrium-type and link-type lattice Boltzmann models for generic advection and anisotropic-dispersion equation," Adv. Water Resour **28**, 1171–1195 (2005).

[31] I. Ginzburg, D. D'Humières, and A. Kuzmin, "Optimal stability of advection-diffusion lattice Boltzmann models with two relaxation times for positive/negative equilibrium," J. Stat. Phys. **139**, 1090–1143 (2010).

[32] R. Allen and T. Reis, "Moment-based boundary conditions for lattice Boltzmann simulations of natural convection in cavities," Prog. Comp. Fluid Dyn.: An Int. J. **16**, 216–231 (2016).

[33] S. Bennett, P. Asinari, and P. Dellar, "A lattice Boltzmann model for diffusion of binary gas mixtures that includes diffusion slip," Int. J. Numer. Meth. Fluids **69**, 171–189 (2012).

[34] A. Hantsch, T. Reis, and U. Gross, "Moment method boundary conditions for multiphase lattice Boltzmann simulations with partially-wetted walls," J. Comput. Multiphase Flows **7**, 1–14 (2015).

[35] S. Mohammed and T. Reis, "Using the lid-driven cavity flow to validate moment-based boundary conditions for the lattice Boltzmann equation," Arch. Mech. Eng. **64**, 57–74 (2017).

[36] T. Reis, "Burnett order stress and spatially-dependent boundary conditions for the lattice Boltzmann method," Commun. Comp. Phys. **27**, 167–197 (2020).

[37] T. Reis and P. Dellar, "Moment-based formulation of Navier–Maxwell slip boundary conditions for lattice Boltzmann simulations of rarefied flows in microchannels," Phys Fluids (2012).

[38] A. Pasquali, M. Geier, and M. Krafczyk, "Near-wall treatment for the simulation of turbulent flow by the cumulant lattice boltzmann method," Computers and Mathematics with Applications **79**, 195 – 212 (2020).

[39] K. Kutscher, M. Geier, and M. Krafczyk, "Multiscale simulation of turbulent flow interacting with porous media based on a massively parallel implementation of the cumulant lattice boltzmann method," Computers and Fluids **193**, 103733 (2019).

[40] D. D'Humiéres and I. Ginzburg, "Viscosity independent numerical errors for lattice Boltzmann models: from recurrence equations to"magic" collision numbers," Comput. Math. Appl. **58**, 823–840 (2009).

[41] T. Reis, "On the lattice Boltzmann deviatoric stress: Analysis, boundary conditions, and relaxation times," Submitted to SIAM J. Sci. Comput. ((2018)).

[42] S. Chapman and T. G. Cowling, *The mathematical theory of non-uniform gases: an account of the kinetic theory of viscosity, thermal conduction and diffusion in gases* ((Cambridge Univ Press, Cambridge, England, 1970).

[43] X. He, X. Shan, and G. Doolen, "Discrete Boltzmann equation model for nonideal gases," Phys. Rev. E **57**, R13 (1998).

[44] S. Bennett, *A lattice Boltzmann model for diffusion of binary gas mixtures*, Ph.D. thesis, University of Cambridge (2010).